UNIVERSITY OF CALIFORNIA, SAN DIEGO

Nanoscale Light Confinement: Bowtie Antenna and Perfect Absorbers

A Thesis submitted in partial satisfaction of the requirements for the degree Masters of Science

In

NanoEngineering

by

David Alexander Rosen

Committee in charge:

Professor Andrea Tao, Chair
Professor Eric Fullerton
Professor Donald Sirbuly

2014

The Thesis of David Alexander Rosen is approved and it is acceptable in the quality and form for publication on microfilm and electronically:

Chair

University of California, San Diego

2014

Dedicated to my mother and father for always supporting me, and to my brother for all of his help in all aspects of life.

TABLE OF CONTENTS

LIST OF FIGURES

LIST OF SCHEMES

ACKNOWLEDGEMENTS

Chapter 2, in full is reprint of the material as it appears in ACS Applied Materials and Interfaces 2014. Rosen, David; Tao, Andrea. The Thesis author was the primary investigator and author of this material.

Chapter 3, in part is a reprint of material that is being prepared for submission. Rozin, Matthew, Rosen, David, Tao, Andrea. The Thesis author was the secondary investigator of this material.

ABSTRACT OF THE THESIS

Nanoscale Light Confinement: Bowtie Antenna and Perfect Absorbers

by

David Alexander Rosen

Master of Science in NanoEngineering

University of California, San Diego, 2014

Professor Andrea Tao, Chair

The confinement of light in cavities that are smaller than the optical diffraction limit can be achieved through the use of metallic nanoparticles by exploiting their optical properties. Two geometries were studied for their different capabilities of light

confinement. First, a bowtie nanojuction which provides high localization to the gap created between two triangular prisms. Second, a metal-insulator-nanoparticle sandwich structure which localizes light to the gap between two metal films. Simulations were widely utilized to model the optical properties of each geometry. For bowtie antenna finite element method (FEM) was used to model the effect of defects that occurs as the result of nanoparticle synthesis or the assembly into bowties. It was found that defects have the ability to shift the resonant wavelength by as much as 200 nm. Bowtie junctions also demonstrated defect tolerance with respect to the near-field enhancement providing evidence that they will be viable structures for nanophotonic and nanoplasmonic applications. For the sandwich structure, also known as a nanocube metasurface, finite difference time domain (FDTD) was used to model the plasmonic mode structure of the metasurface. Through simulation and experimental findings it was found that the metasurface provides nearly perfect absorbance at its resonant frequency, confining the light to nanoparticle-nanoparticle gaps, and the nanoparticle-film gap. The addition of a gain medium to the insulating spacer layer is also being explored. It holds promise for fluorescence enhancement and sensing applications.

1. Introduction

1.1 Plasmonics

Nanoparticle production and assembly has gained interest in the scientific community. This interests stems from the unique optical and physical properties of nanoparticles that has prospective uses in a broad range of applications. Plasmonic particles have been at the forefront of this interest due to their light focusing and enhancing properties. At a bulk scale plasmons are excited at the surface of a material. In this case the conduction electron at the surface are able to oscillate at the frequency of incoming light. The oscillation of the electrons creates propagating surface plasmon polaritons at the interface between the plasmonic material and the dielectric. Generally plasmons or surface plasmon polaritons are only excitable through the use of a metal and an exterior prism in the Otto or Kretschmann configuration, though other methods, such as using a grating or roughened surface have been used experimentally.[1] When a dimension of the excited surface is brought into the nanoscale (< 250 nm) localized surface plasmons resonances (LSPR) are observed. In the case of a LSPR the conduction electrons of the metal are able to oscillate at the same frequency as the incoming electromagnetic wave throughout the volume of the particle. The small scale and inherent geometry of the nanoparticle allows the plasmon to be excited without the presence of a prism, though a neighboring dielectric (including vacuum) is required. Localized surface plasmons resonances are sensitive to a whole host of factors. This makes nanoparticle resonances and enhancements highly tunable for use in applications covering the whole visible spectrum and continuing into the

infrared. Particle size, shape and orientation in relation to the polarization angle of the incident light all cause the shifting of LSPR. The dielectric environment also has the ability to alter the resonance of a plasmonic nanoparticle.

1.2 Top-down and Bottom-up Manufacturing

There are two disciplines of study for the synthesis of plasmonically active nanoparticles. These are top-down manufacturing, and bottom up assembly or growth. Top-down manufacturing involves the removal of a bulk substance in order to form a nanoscale particle. This is often done in a clean room, utilizing an electron beam writer. Photolithography, focused ion beam, and laser ablation are more example of top-down manufacturing techniques. These techniques have the advantage of being highly controllable. In most cases the operator has precise control over the location and orientation of the nanoparticle. A downside to top-down technology is that it is limited by the resolution of the device and that it tends to be slow and costly.

Conversely bottom-up techniques build up nanoparticles from smaller building blocks such as individual atoms. Nanoparticles that are build bottom-up can usually be synthesized in a simple wet chemistry lab. Several groups have shown to have both excellent size and shape control when synthesizing the particles.[2] Chemically synthesized particles also tend to be more crystalline then particles that be been fabricated through top-down processes.[3] A major issue with top-down synthesis is the limited ability in the placement and orientation of the particles on a substrate or three-dimensional array. While both methods have their advantages and challenges bottom-up growth and assembly of

nanoparticles shows the most promised because of the low cost and high throughput of the nanoparticle production.

1.3 Nanoparticle Geometries

Various geometries have been studied to provide improved optical characteristics. One such geometry is the bowtie antenna. The bowtie antenna is formed by bring two triangular prisms close together in a bowtie like fashion.[4] The sharp features of the prism result in high electric field generation at the vertices when the LSPR mode is excited. Further so, when two prisms are brought within a few nanometers of each other the plasmons couple and result in an electric field enhancement in the gap that can greatly exceed that of a single particle. These particles bowtie particles are being explored for uses as optical antennas for sensing,[5] nanoscale lasing[6] and non-diffraction limited photolithography.[7]

Another geometry that has been studied here is a sandwich structure or metasurface, in which a dielectric layer is placed between a gold or silver thin film and a close-packed array of plasmonic particles. From this geometry coupling occurs between the particles themselves, as well as the particles and the metal film. The resultant cavity has the ability to nearly perfectly absorb light at the resonant plasmon frequency. As a consequence of the absorption, the metasurface is being explored for use in applications such as photovoltaics,[8] and selective thermal emission.[9] An interesting extension of this structure is obtained when a gain media is added to the dielectric layer that is between the metal film and the nanoparticles. Gain media normally seen in lasers have been shown to have a positive interaction with plasmons enhancing both the electric field strength and lifetime of the

plasmon.[10] In addition the enhanced electric field caused by the plasmon can result in higher fluorescence intensities and shorter decay times.[11] Also with the addition of a gain media the opportunity for nanoscale lasing is evident.[12] A gain medium normally consists of a fluorescent organic dye or fluorescent semiconductor nanoparticles known as quantum dots.

1.4 Chapter 1 References

(1) Maier, S. A. *Plasmonics : Fundamentals and Applications*; Springer: New York, 2007; p. xxiv, 223 p.

(2) Tao, A. R.; Habas, S.; Yang, P. Shape Control of Colloidal Metal Nanocrystals. *Small* **2008**, *4*, 310–325.

(3) Huang, W.; Qian, W.; El-sayed, M. A.; Ding, Y.; Wang, Z. L. Effect of the Lattice Crystallinity on the Electron - Phonon Relaxation Rates in Gold Nanoparticles. *J. Phys. Chem. C* **2007**, 10751–10757.

(4) Kim, S.; Jin, J.; Kim, Y.-J.; Park, I.-Y.; Kim, Y.; Kim, S.-W. High-Harmonic Generation by Resonant Plasmon Field Enhancement. *Nature* **2008**, *453*, 757–760.

(5) Hatab, N. A.; Hsueh, C.-H.; Gaddis, A. L.; Retterer, S. T.; Li, J.-H.; Eres, G.; Zhang, Z.; Gu, B. Free-Standing Optical Gold Bowtie Nanoantenna with Variable Gap Size for Enhanced Raman Spectroscopy. *Nano Lett.* **2010**, *10*, 4952–4955.

(6) Yu, N.; Cubukcu, E.; Diehl, L.; Bour, D.; Corzine, S.; Zhu, J.; Höfler, G.; Crozier, K. B.; Capasso, F. Bowtie Plasmonic Quantum Cascade Laser Antenna. *Opt. Express* **2007**, *15*, 13272–13281.

(7) Sundaramurthy, A.; Schuck, P. J.; Conley, N. R.; Fromm, D. P.; Kino, G. S.; Moerner, W. E. Toward Nanometer-Scale Optical Photolithography: Utilizing the Near-Field of Bowtie Optical Nanoantennas. *Nano Lett.* **2006**, *6*, 355–360.

(8) Moreau, A.; Ciracì, C.; Mock, J. J.; Hill, R. T.; Wang, Q.; Wiley, B. J.; Chilkoti, A.; Smith, D. R. Controlled-Reflectance Surfaces with Film-Coupled Colloidal Nanoantennas. *Nature* **2012**, *492*, 86–89.

(9) Mason, J. a.; Smith, S.; Wasserman, D. Strong Absorption and Selective Thermal Emission from a Midinfrared Metamaterial. *Appl. Phys. Lett.* **2011**, *98*, 241105.

(10) Liu, N.; Wei, H.; Li, J.; Wang, Z.; Tian, X.; Pan, A.; Xu, H. Plasmonic Amplification with Ultra-High Optical Gain at Room Temperature. *Sci. Rep.* **2013**, *3*.

(11) Gather, M. C.; Meerholz, K.; Danz, N.; Leosson, K. Net Optical Gain in a Plasmonic Waveguide Embedded in a Fluorescent Polymer. *Nat Phot.* **2010**, *4*, 457–461.

(12) Noginov, M. a; Zhu, G.; Belgrave, a M.; Bakker, R.; Shalaev, V. M.; Narimanov, E. E.; Stout, S.; Herz, E.; Suteewong, T.; Wiesner, U. Demonstration of a Spaser-Based Nanolaser. *Nature* **2009**, *460*, 1110–1112.

2. Modeling the Optical Properties of Bowtie Antenna Generated By Self-Assembled Ag Triangular Nanoprisms

2.1 Introduction

Metal nanostructures composed of Au and Ag behave like optical antennae by supporting the excitation of localized surface plasmon resonances (LSPRs), where conduction electrons of the metal oscillate in resonance with incident light to produce intense electromagnetic fields localized at the metal surface. Metal nanostructure size, shape, and arrangement are critical in determining the LSPR wavelength and the magnitude of the resulting field enhancement. *Hot spots*, where the electromagnetic field is highly confined within a small volume, are particularly pronounced at sharp nanoscale features (i.e. the antenna effect) and small gaps between adjacent metal surfaces. Recent work has focused on tailoring hot spot properties by thoughtfully designing metal nanostructures with anisotropic geometries such as bowtie antennas,[1] nanoholes,[2,3] triangle arrays formed by nanosphere lithography,[4,5] and nanocrescents.[6,7] These geometries can be produced using top-down approaches such as e-beam lithography as in the case of bowties, or by using template-directed deposition of metal such as nanosphere lithography.

In contrast to these fabrication techniques, self-assembly approaches are advantageous because they can be carried out on a massively parallel scale to generate complex architectures using metal nanocrystal building blocks. Colloidal metal nanocrystals can be synthesized in large batches by wet chemical synthesis and typically possess crystallographically defined facets, edges and corners that enable geometry-

specific coordination. We recently demonstrated that plasmonic hot spots can be fabricated using a bottom-up approach by assembling Ag nanocubes, Au nanorods, and Ag triangular nanoprisms into oriented nanojunctions.[8,9] In this method, shaped Ag or Au nanocrystals are grafted with polymer chains of varying length and chemistries, then embedded within a bulk polymer matrix. Spontaneous phase segregation between polymer and nanocrystal components causes the nanocrystals to assemble into oriented dimers and one-dimensional strings. Hot spots are generated in the nanojunctions (i.e. the gap between nanocrystals) produced by these assemblies.

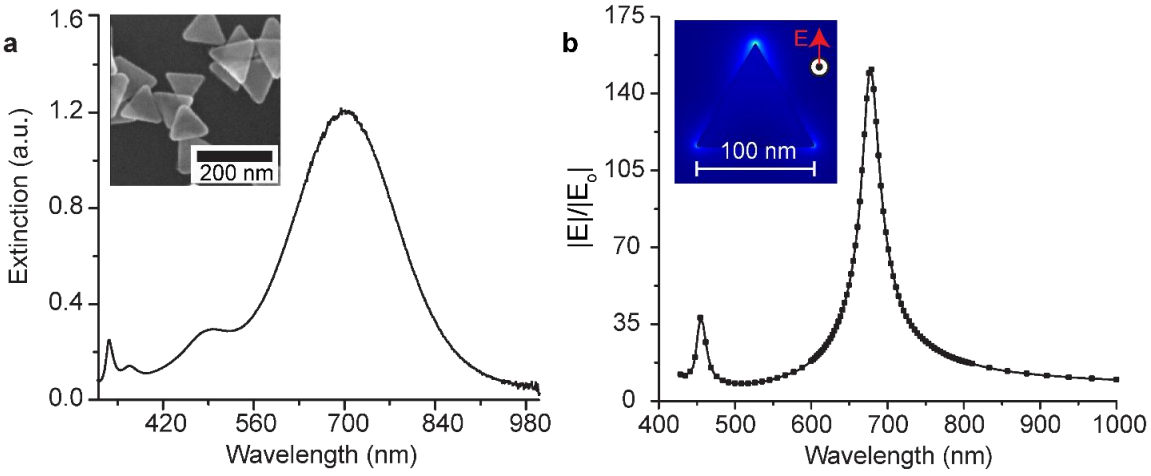

Figure 2.1. (a) UV-Vis extinction spectra of colloidal Ag nanoprisms. Inset shows a SEM image of unassembled nanoprisms. (b) Simulated electric field enhancement ($|E|/|E_o|$) spectra of a single Ag nanoprism. Inset shows the areas of high electric field present at the resonance wavelength of λ=679 nm.

Using the polymer-directed assembly described above, bowtie structures can be fabricated by assembling colloidal triangular Ag nanoprisms. Bowtie antennas are

particularly intriguing plasmonic structures because they are highly polarizable and produce large near-field enhancements within their nanojunction gap. Bowtie structures, or variations of bowtie structures such as inverse bowties,[10] have been used to produce large field enhancements for surface-enhanced Raman spectroscopy,[11] photocatalysis,[12] plasmonic lasers,[13] and single-molecule fluorescence.[14] To assemble bowties, Ag triangular nanoprisms are first synthesized using an aqueous seed-mediated growth method at room temperature. Figure 2.1a shows a typical extinction spectrum for a dispersion of Ag nanoprisms in water, taken by UV-Visible spectroscopy. In agreement with previous reports,[15] the spectrum displays peaks for the in-plane dipolar LSPR mode at λ=699 nm, the in-plane quadrupolar LSPR mode at □=490 nm, and the out-of-plane quadrupolar mode at λ=337 nm. Depending on the reaction time allotted for nanocrystal growth, the side length of the prisms range from 100-150 nm and thicknesses range from 6-10 nm, as seen in the scanning electron microscope (SEM) image in the inset.

Figure 2.1b shows a finite element method (FEM) simulation for an individual Ag triangular nanoprism with a side length of 100 nm, a thickness of 8 nm, and a 1 nm radius of curvature at each of the three prism corners. (See Methodology for more details.) The in-plane dipolar mode occurs at λ=679 nm and the in-plane quadrupolar peak occurs at λ=455 nm, in good agreement with experiment. The out-of-plane quadrupolar mode is not observed because the incident plane wave is polarized in-plane. The inset shows a color map of the near-field distribution for a single prism excited at λ=679 nm. When compared to FEM simulations, the experimental extinction curve for the colloidal sample exhibits considerable broadening of the LSPR peaks, likely due to size and shape dispersity of the

synthesized nanoprisms. Small discrepancies in LSPR wavelength can be attributed to discrepancies in the refractive index of the surrounding medium, since the as-made Ag nanoprisms are capped with a polymer and are suspended in water.

In this investigation, we use modeling to evaluate the near-field and far-field optical properties of bowtie nanoatennas fabricated by nanoprism self-assembly. To build the nanoantennas, nanoprisms are assembled into junctions that possess a tip-to-tip orientation. Figure 2.2a shows a scanning electron microscope (SEM) image of the resulting assembly.[8] The gap sizes produced by this self-assembly method are dictated by the length of the polymer graft, which can range from 2-5 nm. In comparison, the smallest junctions demonstrated for antenna structures generated by e-beam lithography are approximately 10-15 nm wide. Because bowtie antennas are well-studied plasmonic structures, we are able to make a direct comparison between the optical properties of lithographically generated structures and structures generated by nanoprism self-assembly. We use FEM simulations to investigate the optical properties of both perfect and defective nanoprism bowties. We examine the effect of common defects observed in polymer-guided nanoprism assembly, including imperfect nanoprism shape and nanoprism misalignment. We seek to determine the biggest challenges for self-assembly techniques in the manufacturing of large-scale plasmonic films or metamaterials.

2.2 Methodology

We carried out electrodynamic simulations using a commercial finite element method software package (COMSOL Multiphysics). The majority of the simulations were run on a quad core Intel i5 3.3 Ghz processor with 16 GB of RAM. Additional simulations

were run on the San Diego Super Computer Center's Triton Shared Computing Cluster (TSCC). Simulation times ranged from 30 minutes to 12 hours depending on the size of the structure being evaluated. Refractive index data for Ag was interpolated from Johnson and Christy.[16] In all simulations, the nanoprisms are modeled in an air (n=1) environment, and light propagation is taken in the z-direction (out-of-plane). A substrate was not added to ease computational costs. While other studies have clearly indicated that metal nanostructures in direct contact with a dielectric substrate experience substrate effects[17], we do not account for such effects because the self-assembly process utilizes nanoprisms that are distributed in an isotropic polymer medium and no significant substrate effects are exhibited.

Simulations were performed for incident light with wavelengths between 430-1000 nm and electric field strengths of 1 V/m at standard temperature and pressure. Initial simulations were run with a step size of approximately 6 nm; to achieve better spectral resolution near the LSPR wavelength, additional simulations were run with a step size of 2 nm. The initial electric field before the addition of light was set at 0 V/m. A spherical perfectly matched layer (PML) with a radius of 1 μm and a thickness of 300 nm was used to absorb scattered waves and prevent reflective interference. *Extremely fine tetrahedral* meshing was used for the bowtie structure, *Extremely fine* meshing entails a maximum element size of 40 nm, a minimum element size of 0.4 nm, and a maximum element growth rate of 1.3. *Finer* tetrahedral mesh was used for the air surrounding the bowtie. A *Finer* mesh has a maximum element size of 110 nm, a minimum element size of 8 nm and a maximum growth rate of 1.4. The mesh used for the PML was a *Finer* triangular mesh that

was swept across the thickness of the PML. Five layers were used, resulting in a layered shell structure bounding the air and bowtie structure. The scattering boundary condition was set as the outer shell of the PML in each simulation. The far-field domain was defined as the air surrounding the bowtie, while the far-field calculation was carried out at the inner shell of the PML.

The electric field enhancement ($|E|/|E_o|$) for LSPRs corresponding to gap modes was calculated by finding the maximum electric field at the midpoint of each bowtie gap for each frequency point. For misaligned bowtie structures composed of nanoprisms rotated about the gap axis, the maximum electric field was evaluated along the gap axis (defined in Fig. 6a). The field enhancement for non-gap modes (evaluated for single nanoprisms, trimers, and tetramers) were calculated by finding the maximum electric field at a point 2.5 nm away from the nanoprism vertex.

To calculate the scattering efficiency, we first used the COMSOL "far-field calculation" node to calculate the far electromagnetic field, E_{far}. The geometric cross-section (CS_g) was calculated by calculating the surface integral over the top surface of the Ag bowtie structure, upon which light directly impinges:

$$CS_g = \int dA \quad (1)$$

Scattering efficiencies were calculated by integrating the square of the far-field over all space and multiplying by a system dependent constant:[18]

$$Q_{Scat} = \frac{1}{CS_g * {E_o}^2} * \frac{1}{{R_{PML}}^2} * \int {E_{far}}^2 * {R_{PML}}^2 \, d\Omega \quad (2)$$

where CS_g is the geometric cross-section of the bowtie and E_o is the incident electric field strength. R_{PML} is the inner radius of the PML and remains constant at 700 nm for all

simulations. The R_{PML} in the integrand is added automatically by COMSOL as part of its normalization procedures, so we divide by R_{PML}^2 to remove this normalization term. The scattering efficiency is a unit-less term as we are dividing the scattering cross-section (units of area) by the geometric cross-section (units of area).[19] In both the electric field enhancement and the scattering efficiency plots, individual data points were fitted using OriginLab's spline function for visual clarity.

Perfect bowties: Perfect bowtie structures were modeled as two 100 nm triangular nanoprisms with an 8 nm thickness. A 1 nm radius of curvature added to each of the three vertices. Bowties were modeled with a gap size (metal-to-metal distance) of 5 nm. The bowtie structure was placed with the dimer axis along the y-axis of the model coordinate system. The middle of the gap was placed at the coordinate origin (0,0,0), such that the bowtie structure is bisected by the xy-plane and that the xy-plane runs parallel to the basal planes of the nanoprisms. Modeling for both x- and y- polarization was done with light propagating in the z-direction.

Gap distance: Perfect bowtie structures described above were modeled with varying gap distances of 2.5, 5, 10, 20, 40 and 80 nm. Illumination by y-polarized light was exclusively used.

Nanoprism thickness: Perfect bowtie structures described above were modeled with varying nanoprism thicknesses of 8, 12, 16, and 20 nm. Illumination by y-polarized light was used exclusively. For our calculation of scattering efficiencies, it is important to note that even though the volume of the nanoprisms changes, the overall geometric cross-

section (CS_g) used in the calculation remained constant. The location of the middle of the gap remained at (0,0,0) for each thickness.

Rounded corners: Perfect bowties with a gap size of 5 nm and a thickness of 8 nm were modeled with varying nanoprism curvatures. The radius of curvature, r, for each vertex of the nanoprisms were increased until a disk was obtained at r=29 nm. Curvatures of 1, 10, and 20 nm were also modelled. Illumination by y-polarized light was used exclusively. For our calculation of scattering efficiencies, it is important to note that the geometric cross-section of each bowtie was changed significantly with curvature, ranging from 8640 nm^2 for r=1 nm radius of curvature to 5240 nm^2 for r=29 nm.

Misalignment: For misaligned bowtie structures, both prisms in the bowtie were rotated with respect to the perfect bowtie axis (y-axis). Rotation angles of 90-30° were modeled, where a 90° rotation gives a perfect bowtie structure. The gap distance at the closest point between the prisms was held constant at 5 nm. Illumination by y-polarized light was used exclusively. For misaligned bowties, both prisms comprising the dimer were rotated around the inner vertex of the bowtie structure. For this reason, the center of the bowtie gap is not at (0,0,0), but is instead shifted along the x-axis. Electric field enhancement was calculated as the maximum field along a line that bisects bowtie gap. To calculate the field enhancement for LSPR modes not localized to the bowtie gap, we determined the maximum electric field at a distance of 2.5 from the prism outer prism vertexes.

Trimers and Tetramers: To construct a nanoprism trimer, a third nanoprism was added to the perfect bowtie structure. The third prism was orientated so that it formed

another perfect bowtie junction rotated at 30 degrees off of the y-axis with a gap distance of 5 nm. Simulations using x- and y- polarizations were performed. The electric field enhancement was calculated at both the original bowtie gap center (0,0,0), the second gap midpoint, and at each remaining vertex in order to compare the non-gap LSPR modes. The tetramer structures were constructed with a fourth prism added to the trimer structure, forming a third perfect bowtie junction structure with the third nanoprism. In this structure, two of the perfect bowties are parallel to each other. In addition to the outer vertices, the electric field enhancement was again calculated at each gap midpoint.

2.3 Results and Discussion

First, we examined perfect bowtie structures generated by a nanoprism dimer where two nanoprisms are arranged in a tip-to-tip geometry and separated by a distance of 5 nm. Figure 2.2b,c shows cross-sections of the nanoprism bowtie structure taken in the xy-plane at the resonant LSPR wavelengths. Figure 2.2d,e plots the calculated near-field enhancements and the scattering efficiencies for a perfect bowtie with respect to wavelength. For x-polarized light, the peak located at λ=676 nm corresponds to excitation of a dipolar LSPR mode where light is localized to the four equivalent outer vertexes of the bowtie structure, with $|E|/|E_o|$=95 at a distance of 2.5 nm from each corner. As expected, our simulations show hot spot generation within the 5-nm air gap between nanoprisms when incident light is polarized parallel to the dimer axis (y-polarized light). The high degree of light localization in the bowtie gap indicates that this is the main dipolar LSPR mode for the bowtie structure, consistent with LSPR coupling between the closely-spaced nanoprisms. This gap mode exhibits a field enhancement of $|E|/|E_o|$=479 and a large far-

field scattering efficiency of Q_{scat}=19. The spectrum in Figure 2.2d shows two additional peaks at 462 nm and 526 nm corresponding to higher order LSPR modes where the electric near-field is localized to both the gap and to the edges or outer corners of the nanoprisms, respectively. The field enhancement associated with these higher order LSPR modes is significantly smaller the dipolar gap mode, with $|E|/|E_o|$=80 and 61 respectively. These LSPR assignments are consistent with previous modeling efforts for bowtie antenna.[20]

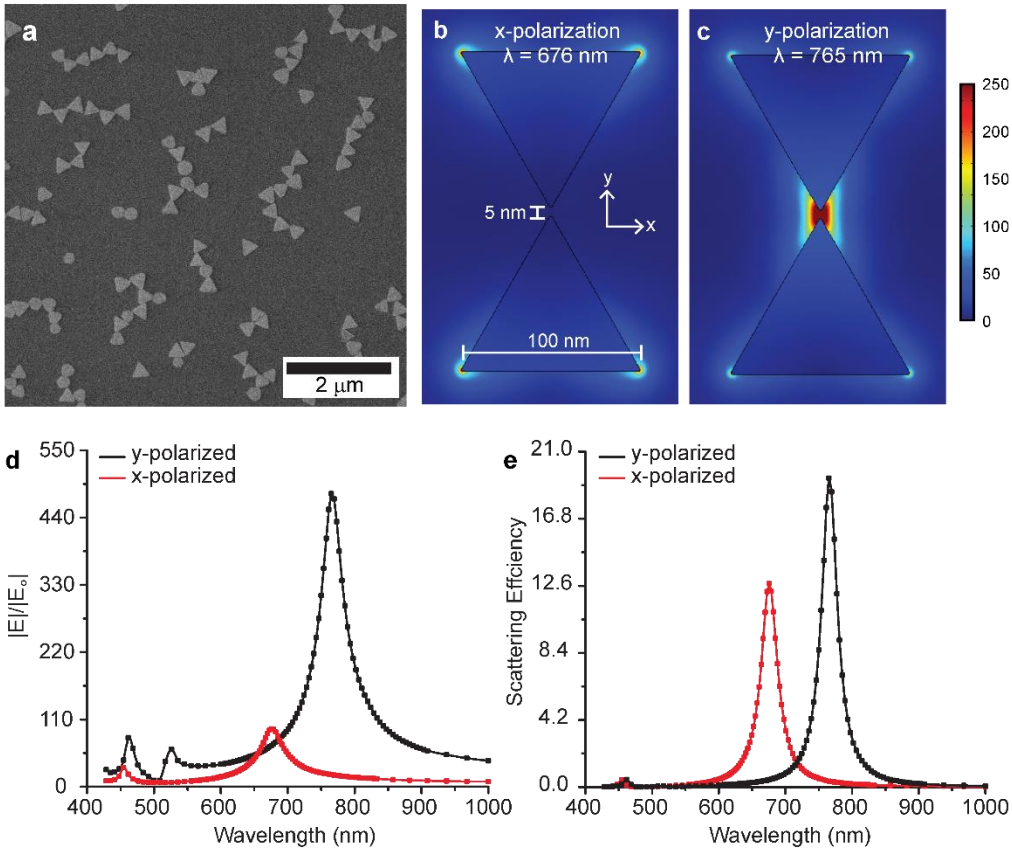

Figure 2.2. (a) SEM image of self-assembled colloidal nanoprisms into bowtie structures. (b,c) Simulated near-field intensities for the perfectly assembled bowtie structure taken in the xy-plane (at z=0) under (b) x-polarization and (c) y-polarization. (d) Calculated wavelength-dependent near-field intensities for the perfectly assembled bowtie structure when illuminated with either x- or y- polarized light. (e) Simulated scattering efficiencies for the perfect bowtie structure obtained for each polarization direction.

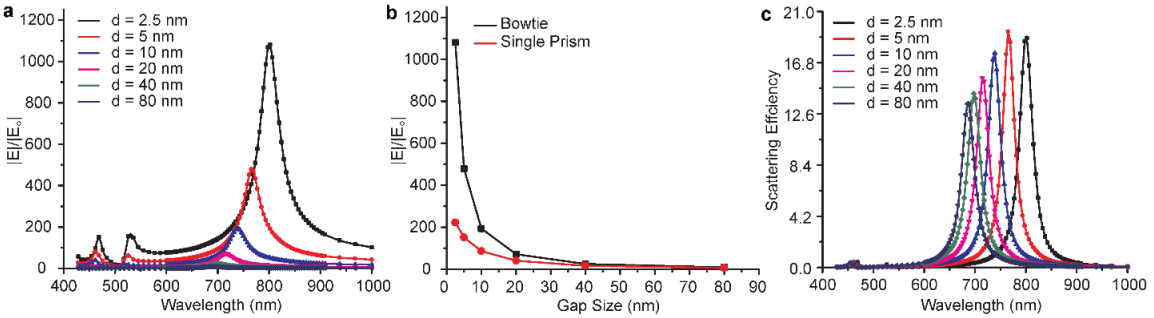

Figure 2.3. (a) Simulated spectra of the changes in $|E|/|E_o|$ as the gap distance of the bowtie structure increases. (b) A plot of the calculated $|E|/|E_o|$ at the mid-gap point versus the bowtie gap distance. Also plotted for comparison is the calculated $|E|/|E_o|$ for a single triangular nanoprism at the equivalent distance away from the prism vertex. (c) Scattering efficiencies of the bowties with respect to increasing gap distance.

In our self-assembly method, the gap distance between nanoprisms is determined by the length of polymer chains that are grafted to the nanoprism surface, which can be between 2-5 nm long. In contrast, lithographic bowtie structures tend to possess gap distances between 5-50 nm. To investigate how this affects light localization within the nanoprism gap, we modeled perfect bowtie structures with varying gap distances of: 2.5, 5, 10, 20, 40, and 80 nm. All simulation parameters were kept the same as the previous simulation, with incident light polarized along the dimer axis. Figure 2.3a shows a plot of the calculated near-field intensities for each gap size and Figure 2.3b shows a plot of the highest $|E|/|E_o|$ for each gap size. We observe two effects: i) near-field enhancement increases as the gap distance decreases, and ii) the resonant wavelength of the gap mode red-shifts as the gap distance decreases. Both observations are consistent with previous descriptions of nanoprism dimers generated by lithography.[21] For a gap distance of 2.5 nm, the LSPR peak exhibits a total redshift of λ=123 nm when compared to the LSPR

wavelength for an isolated triangular nanoprism. Spectral peaks attributed to the excitation of higher order mode LSPR modes do not shift significantly with changing gap size. Figure 2.3b shows that $|E|/|E_o|$ in the bowtie gap decreases exponentially with increasing gap size. Here, strong plasmonic coupling occurs between the two triangular nanoprisms occurs at gap distances < 20 nm at which point the bowtie structure is able to produce more intense hot spots than an isolated triangular nanoprism. For a gap size of 2.5 nm, the calculated field enhancement is $|E|/|E_o|$ =1081. For gap sizes > 20 nm, the maximum $|E|/|E_o|$ within the bowtie gap approaches the field enhancement obtained for a single triangular nanoprism, indicating a loss of coupling. Figure 2.3c shows the scattering efficiencies obtained for the changing gap distances, which shows an expected decrease in scattering efficiency as distance increases. One exception is for scattering efficiency of the bowtie possessing a 2.5 nm gap, which possesses a scattering efficiency that is 0.5 units below the efficiency of the bowtie with the 5 nm gap. In general, strong scattering efficiencies are only exhibited for gap distances <40 nm.

One potential challenge in utilizing colloidal triangular nanoprisms as building blocks for the self-assembly of bowtie antenna structures is the nanoprism thickness. While nanoprism edge length can be tuned by modulating synthetic parameters such as reaction time and reactant concentration,[22,15] the overall thickness of the triangular nanoprisms is difficult to control. Typically, Ag triangular prisms are formed with a thickness of approximately 8 nm, well below the typical metal thickness obtained for top-down fabricated bowtie structures. To evaluate how nanoprism thickness affects the near-field confinement properties of the bowtie antenna, we evaluated perfect bowties with varying

nanoprism thicknesses ranging from 8 nm (a typical value measured for colloidal nanoprisms) to 20 nm (in the range of bowtie thicknesses obtained

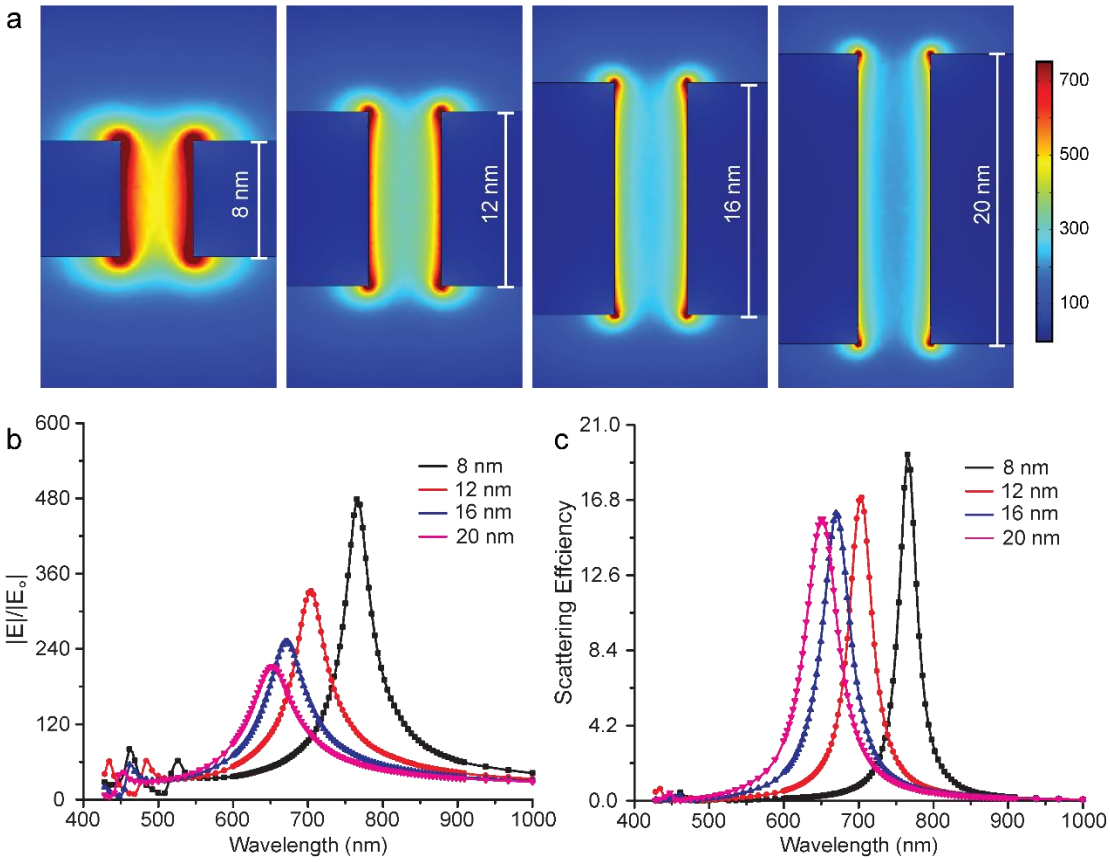

Figure 2.4. (a) Color maps of the near-field intensities in the yz-plane as the thickness of the nanoprisms comprising the assembled bowtie structure in increased. (b) The calculated $|E|/|E_o|$ and (c) corresponding far-field scattering efficiency spectra for the bowtie structure as the thickness of the nanoprism is increased from the measured nanoprism thickness of 8 nm to 20 nm, a typical value for structures templated by photolithography.

by electron-beam lithography). Figure 2.4a shows color maps of the calculated near-field intensities for the dipolar gap mode for the nanoprism thicknesses of 8, 12, 16, and 20 nm. The images show cross-sections taken in the yz-plane. Figure 2.4b,c show plots of the near-field intensities and scattering efficiencies of the bowtie structures. As the thickness of the

Ag nanoprism increases, |E|/|Eo| in the gap decreases significantly and the LSPR wavelength of gap mode blue-shifts. The thinnest bowtie structure (8 nm) exhibited the highest near-field enhancement with |E|/|Eo|=479 at λ=765 nm. Increasing the bowtie thickness to 12 nm causes this value to fall to 70 % of its value, with |E|/|Eo|=332 at λ=704 nm. The thickest bowtie antennae we investigated (20 nm) resulted in a field enhancement of |E|/|Eo|=212 at λ_{LSPR}=652 nm. This decrease in |E|/|Eo| occurs because the overall illuminated surface area of the bowtie structure remains the same regardless of nanoprism thickness. Thus, any confined light within the gap is distributed over a gap volume that scales with both gap distance and nanoprism thickness. Thickness also has a minimal effect on the far-field scattering efficiency of the bowtie structures, as seen in Figure 2.4c.

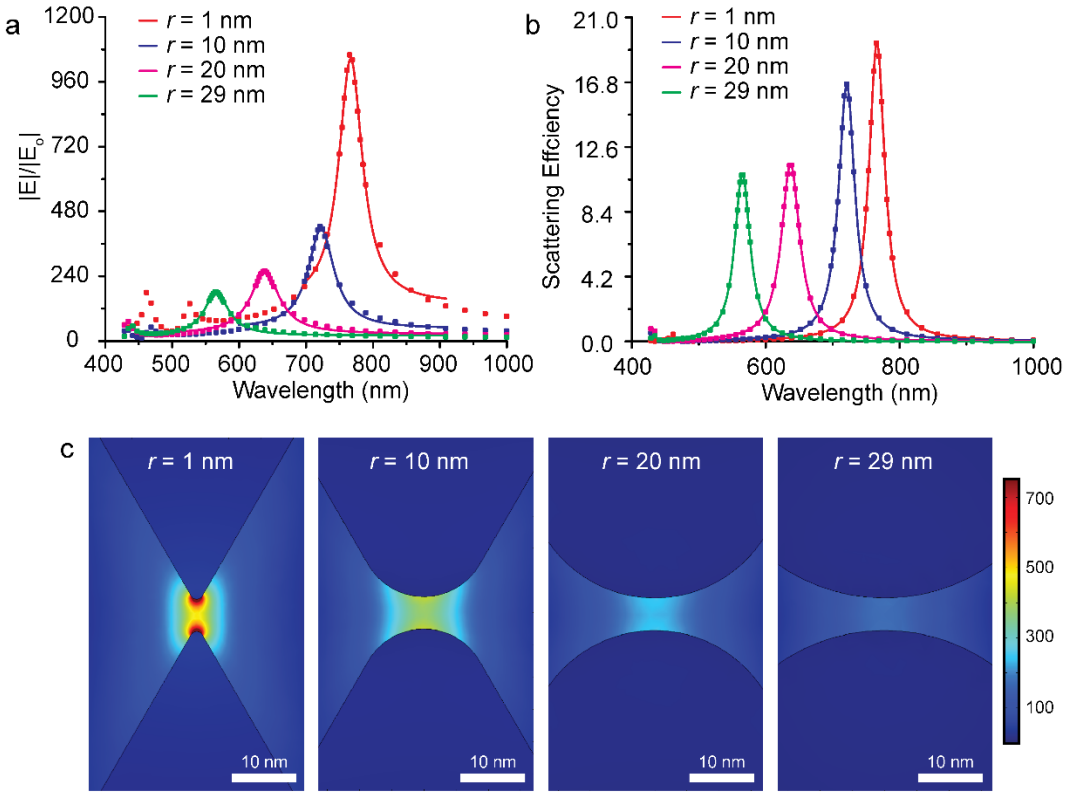

Figure 2.5. (a) Calculated spectra of $|E|/|E_o|$ and (b) corresponding far-field scattering efficiencies for the Ag nanoprism-based bowtie antennae as the radii of curvature of the nanoprism vertexes are increased. (c) Confinement of the electric field in the xy-plane each with increasing radius of curvature.

One of the most common defects observed for nanoprism colloids is rounding and truncation of the prism corners. The Ag surfaces of prism corners possess a high surface energy due to undercoordinated surface atoms and nanoprisms often undergo aging or ripening processes where this rounding becomes more pronounced. In severe cases, rounding results in the formation of Ag disks. To investigate how these rounding defects affect the light confining ability of the bowtie antenna, we carried out simulations for bowtie structures composed of nanoprisms that possess corners with varying radii of curvature. We varied the radius of curvature from a minimum of r=1 nm representing

nanoprisms with sharp triangular corners, to a maximum of *r*=29 nm at which point the prisms lose their in-plane anisotropy and become circular disks. Figure 2.5a,b plots the near-field strength and scattering efficiency of each rounded bowtie structure and Figure 2.5c shows a color map of the corresponding near-field intensities. These maps are cross-sections that are taken in the xy-plane. As the radius of curvature increases, the near-field enhancement associated with the bowtie gap mode decreases and that the dipolar gap mode exhibits a blueshift in LSPR wavelength by over 200 nm. While the scattering efficiencies display only a 44% change for complete rounding of the nanoprism corners, the drop in near-field strength is almost an order of magnitude difference.

Next, we examine the effects of misalignment on the efficacy of bowtie antennas. In our self-assembly strategy, triangular nanoprisms assemble with a wide range of angles that are off the axis of a perfect tip-to-tip nanoprism dimer. Here, we define the structure of the bowtie by the angle of rotation between the bisecting line of the bowtie gap (along the x=0 line in Figure 2.6a and the bisector of the nanoprism (along the y=0 line in Figure 2.6a). In a perfect bowtie dimer, the nanoprisms are rotated at 90° angles with respect to the gap axis. (Figure 2.6b) The nanoprisms can adopt a perfectly misaligned structure where the nanoprisms are rotated 30° with respect to

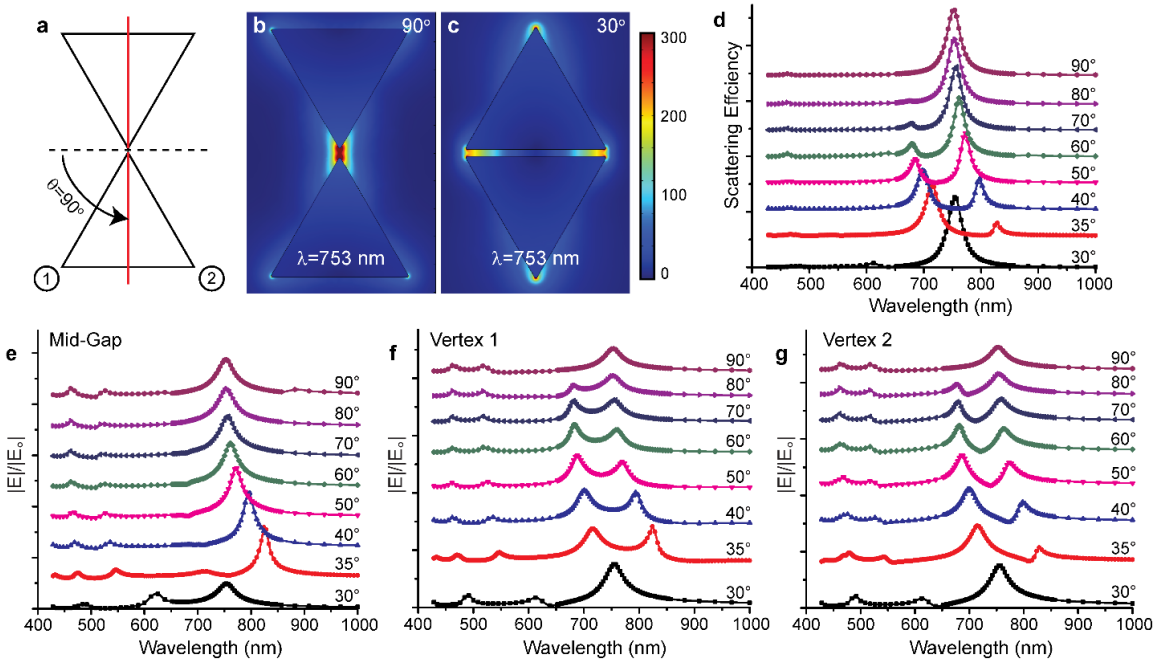

Figure 2.6. (a) Schematic showing how rotation of misaligned bowtie structures is determined by taking the angle θ between the gap bisector and the nanoprism bisector. A perfect bowtie structure corresponds to θ=90°. (b,c) Color maps of the near-field intensities in the xy plane of bowtie structures corresponding to (b) the perfect bowtie dimer with θ=90°, and (c) the misaligned structure with θ=30°. (e-g) Calculated wavelength-dependent and angle-dependent near-field intensities for misaligned bowtie antenna at three different points located 2.5 nm away from the Ag surface: (e) in the middle of the bowite gap, (f) at Vertex 1 or the inner vertex of the misaligned bowtie, and (g) at Vertex 2 or the outer vertex of the misaligned bowtie.

the gap in an edge-to-edge arrangement. (Figure 2.6c) To investigate the effects of such misalignment, we modeled nanoprism dimers that adopt various angle of rotation between 30-90°. Figure 2.6d shows plots of the far-field scattering efficiencies for each off-axis bowtie structure. As the nanoprisms are rotated off the dimer axis from a perfect bowtie structure at 90° to an edge-to-edge structure at 30°, the resonant LSPR wavelength of the dipolar gap mode red-shifts from λ=765 nm to λ=893 nm and decreases in intensity.

Simultaneously, a second spectral peak appears at a shorter wavelength; for the 70° bowtie structure, this peak appears at λ=679 nm. As the rotation angle decreases toward 30°, this second peak red-shifts to λ=714 nm and increases in intensity. Finally, upon perfect misalignment at 30°, the bowtie spectrum exhibits only a single dipolar mode with a peak at of λ=754 nm. This comes from light confinement along the slot generated by the two parallel nanoprisms facets. (Figure 2.6c) In this edge-to-edge arrangement, near-field intensity is not localized in the center of the gap, but rather, at the two outer ends of the gap. Figure 2.6e-g show the wavelength-dependent near-field enhancements at three different locations in the nanoprism bowtie structure: in the center of the gap, at the inner vertex of a misaligned bowtie (designated Vertex 1), and at the outer vertex of a misaligned bowtie (designated Vertex 2).

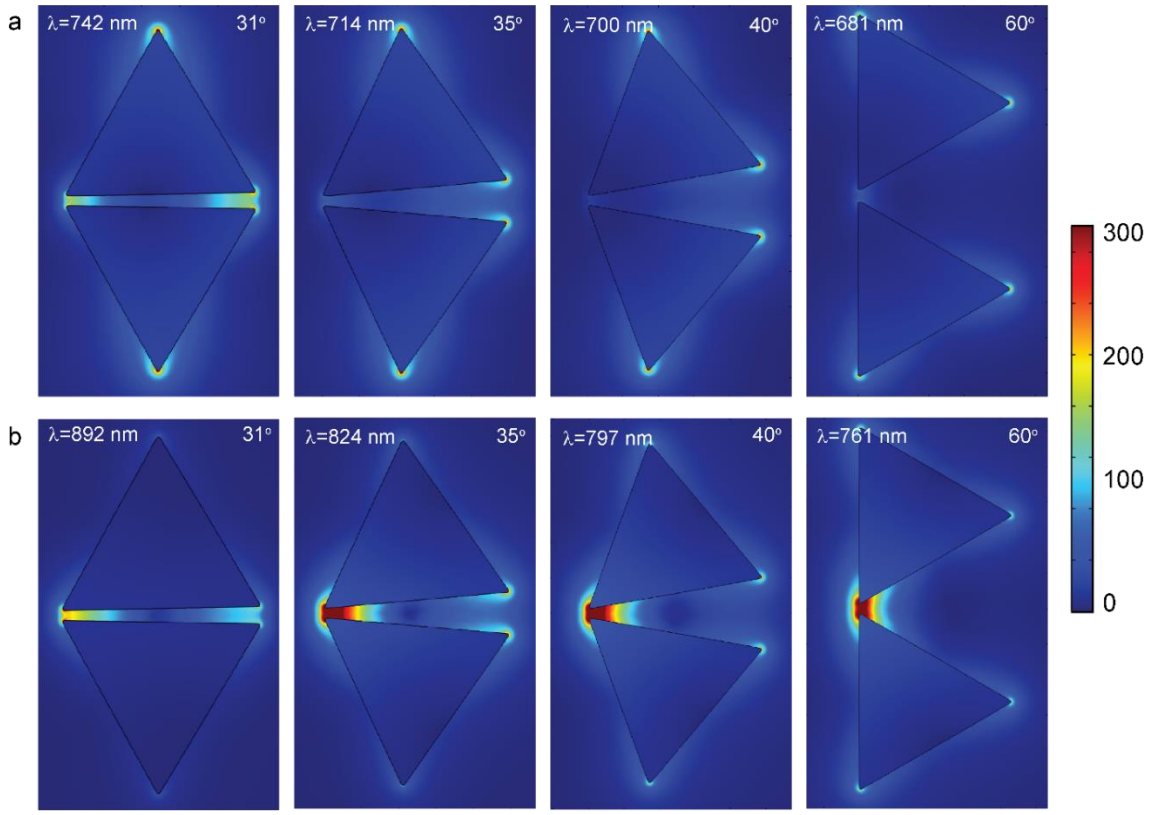

Figure 2.7. Color maps of the calculated near-field intensities for misaligned bowtie antenna. All images are taken as the cross-section of the bowtie structure with the xy-plane. The color maps show the near-field intensities for (a) the higher-order resonance generated by prism rotation, and (b) the fundamental gap mode of the bowtie structure at selected angles of rotation.

Figure 2.7 shows the color maps of the near-fields for misaligned nanoprisms with angles of rotation between 31-60° for the two major spectral peaks that appear in Figure 2.6. These maps show that the two peaks correspond to LSPRs associated with different corners of the bowtie structure. The lower wavelength resonance redshifts from 681 nm to 742 nm with increasing misalignment from 60° to 31° and corresponds to a dipolar LSPR mode associated with hot spot formation at the outer corners of the bowtie structure. In a

perfect bowtie structure, this mode is only excited with x-polarized light and misalignment of the nanoprisms causes this mode to appear when the bowties are excited with y-polarized light. The higher wavelength resonance blue shifts from 765 nm to 892 nm with increasing misalignment and corresponds to the fundamental gap mode of the bowtie structure. The electric field localization for this mode remains considerably high ($|E|/|E_o|=626$) even when the bowties are rotated at 35°. Based on the scattering spectra in Figure 2.6d, we expect that the far-field scattering response of self-assembled nanoprisms displaying a large number of these rotational defects with large angle dispersions will display a broad peak in the 700-800 nm range.

Another assembly defect commonly observed in our polymer-directed assembly method is the formation of trimer and tetramer species. We modeled the effect of these additional nanoprisms on the electric field enhancement and resonant LSPR wavelengths of the nanojunctions associated with these nanoprism clusters. Figure 2.8a shows the near-field enhancement spectra for the trimer structure, which is modelled as three nanoprisms arranged at perfect 90°-angle bowtie junctions. Three major spectral peaks appear, excluding the higher order modes present in the 400-550 nm range. These peaks appear at 676, 735, and 794 nm for

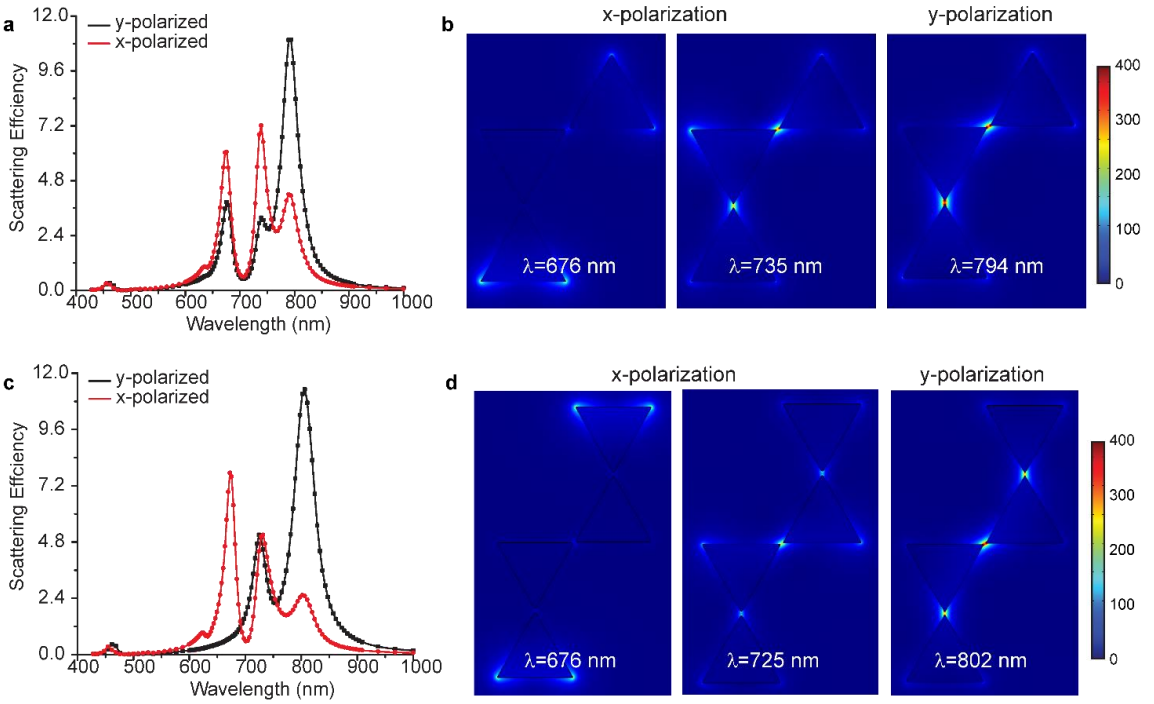

Figure 2.8. (a) Calculated far-field scattering efficiency spectra for a nanoprism trimer composed of three nanoprisms oriented into θ=90° bowtie junctions under illumination with both x- and y-polarized light. (b) Color maps of the calculated near-field intensities for the trimer at the strongest resonances, as indicated by the spectral peaks in (a). (c) Calculated far-field scattering efficiency spectra for a nanoprism tetramer composed of four nanoprisms oriented into θ=90° bowtie junctions under illumination with both x- and y-polarized light. (d) Color maps of the calculated near-field intensities for the tetramer at the strongest resonances indicated by the spectral peaks in (c).

both x- and y- polarization. Figure 2.8b shows the corresponding color plots of the near-field intensities associated with the trimer, from which it is apparent that the dominant peak at λ=794 nm peak corresponds to a dipolar gap mode where light localization occurs in both junctions of the trimer. The off-center axis of the third nanoprism allows the excitation of this mode with both x- and y-polarized light, where $|E|/|E_o|$= 210 for x-polarization and $|E|/|E_o|$=331 for y-polarization. This LSPR mode is red shifted by approximately 29 nm from the major dipolar LSPR peak associated with the perfect bowtie dimer.

The tetramer structure (Figure 2.8c,d) exhibits major spectral peaks at 676, 725, and 802 nm. The color plots in Figure 2.8d show the near-field localization for LSPR excitation at these wavelengths, which indicate the excitation similar symmetric LSPR modes as the trimer. Specifically, the peak at □=802 nm corresponds to a dipolar mode where light localization occurs in all three junctions of the tetramer. Analysis of the near-field enhancement at different vertexes along both the trimer and tetramer structures show that the minor spectral peaks are more difficult to deconvolute than for bowtie dimers, and stem from field localization at multiple locations along each oligomer structure. However, these simulations indicate excitation of LPSR modes where light confinement occurs between nanoprism junctions should occur in a relatively narrow wavelength region (790-805 nm) for small clusters composed of three or four nanoprisms.

2.4 Conclusion

We carried out electromagnetic simulations for Ag bowtie structures that are composed of self-assembled triangular nanoprisms synthesized by colloidal methods. Our simulations suggest that the small gap sizes (<5 nm) provided by self-assembly methods and the ability to fabricate bowtie structures that are extremely thin (~8 nm) are advantageous to the construction of intense electromagnetic hot spots. We examine common defects observed in these self-assembled structures, including rounded nanoprism corners, rotational misalignment and trimer/tetramer formation. Based on this data, we expect that the far-field optical scattering response for self-assembled nanoprisms will display broad peaks in the 600-800 nm due to structural heterogeneities presented by these defects. This may present difficulties for the use of self-assembled in applications where

light reflection or transmission are important. However, the near-field response for both perfect and defective bowtie structures built from Ag nanoprisms is consistent, with the formation of an intense hot spot with $|E|/|E_o| > 200$ at the midpoint between adjacent nanoprisms. The only cases for which this does not occur are bowties formed with defective nanoprisms that possess round, blunt vertexes. This suggests that for self-assembly to be a viable technique for manufacturing bowtie nanoantenna structures, appropriate surface passivation strategies must be developed to prevent shape degradation and promote long-term surface stability. One area which we did not explicitly model in this study is the effect long-range alignment and orientation over multiple bowtie structures. Our results indicate that the polarization direction of incident light relative to the bowtie axis plays a critical role in near-field enhancement associated with the self-assembled structures. Future simulation work probing the relative orientations of multiple bowtie structures may be useful in evaluating the utility of self-assembled nanoprisms for applications where large arrays of bowtie antennae are desired.

Chapter 2, in full is reprint of the material as it appears in ACS Applied Materials and Interfaces 2014. Rosen, David; Tao, Andrea. The Thesis author was the primary investigator and author of this material.

2.5 Chapter 2 References

(1) Kim, S.; Jin, J.; Kim, Y.-J.; Park, I.-Y.; Kim, Y.; Kim, S.-W. Highharmonic generation by resonant plasmon field enhancement. *Nature* **2008**, 453 (7196), 757−760.

(2) Lesuffleur, A.; Kumar, L. K. S.; Gordon, R. Enhanced second harmonic generation from nanoscale double-hole arrays in a gold film. *Appl. Phys. Lett.* **2006**, 88 (26), 261104−1−3.

(3) van Nieuwstadt, J. A. H.; Sandtke, M.; Harmsen, R. H.; Segerink, F. B.; Prangsma, J. C.; Enoch, S.; Kuipers, L. Strong Modification of the Nonlinear Optical Response of Metallic Subwavelength Hole Arrays. *Phys. Rev. Lett.* **2006**, 97 (14), 146102−1−4.

(4) Haynes, C. L.; Van Duyne, R. P. Nanosphere Lithography: A Versatile Nanofabrication Tool for Studies of Size-Dependent Nanoparticle Optics. *J. Phys. Chem. B* **2001**, 105 (24), 5599−5611.

(5) Jensen, T. R.; Malinsky, M. D.; Haynes, C. L.; Van Duyne, R. P. Nanosphere Lithography: Tunable Localized Surface Plasmon Resonance Spectra of Silver Nanoparticles. *J. Phys. Chem. B* **2000**, 104 (45), 10549−10556.

(6) Ross, B. M.; Lee, L. P. Plasmon tuning and local field enhancement maximization of the nanocrescent. *Nanotechnology* **2008**, 19 (27), 275201.

(7) Bukasov, R.; Shumaker-Parry, J. S. Highly Tunable Infrared Extinction Properties of Gold Nanocrescents. *Nano Lett.* **2007**, 7 (5), 1113−1118.

(8) Gao, B.; Alvi, Y.; Rosen, D.; Lav, M.; Tao, A. R. Designer nanojunctions: orienting shaped nanoparticles within polymer thinfilm nanocomposites. *Chem. Commun.* **2013**, 49 (39), 4382−4384.

(9) Gao, B.; Arya, G.; Tao, A. R. Self-orienting nanocubes for the assembly of plasmonic nanojunctions. *Nat. Nanotechnol.* **2012**, 7 (7), 433−437.

(10) Guo, H.; Meyrath, T. P.; Zentgraf, T.; Liu, N.; Fu, L.; Schweizer, H.; Giessen, H. Optical resonances of bowtie slot antennas and their geometry and material dependence. *Opt. Express* **2008**, 16 (11), 7756−7766.

(11) Hatab, N. A.; Hsueh, C.-H.; Gaddis, A. L.; Retterer, S. T.; Li, J.-H.; Eres, G.; Zhang, Z.; Gu, B. Free-Standing Optical Gold Bowtie Nanoantenna with Variable Gap Size for Enhanced Raman Spectroscopy. *Nano Lett.* **2010**, 10 (12), 4952−4955.

(12) Sundaramurthy, A.; Schuck, P. J.; Conley, N. R.; Fromm, D. P.; Kino, G. S.; Moerner, W. E. Toward Nanometer-Scale Optical Photolithography: Utilizing the Near-Field of Bowtie Optical Nanoantennas. *Nano Lett.* **2006**, 6 (3), 355−360.

(13) Yu, N.; Cubukcu, E.; Diehl, L.; Bour, D.; Corzine, S.; Zhu, J.; Höfler, G.; Crozier, K. B.; Capasso, F. Bowtie plasmonic quantum cascade laser antenna. *Opt. Express* **2007**, 15 (20), 13272−13281.

(14) Kinkhabwala, A.; Yu, Z.; Fan, S.; Avlasevich, Y.; Mullen, K.; Moerner, W. E. Large single-molecule fluorescence enhancements produced by a bowtie nanoantenna. *Nat. Photonics* **2009**, 3 (11), 654−657.

(15) Jin, R.; Cao, Y.; Mirkin, C. A.; Kelly, K. L.; Schatz, G. C.; Zheng, J. G. Photoinduced Conversion of Silver Nanospheres to Nanoprisms. *Science* **2001**, 294 (5548), 1901−1903.

(16) Johnson, P. B.; Christy, R. W. Optical Constants of the Noble Metals. *Phys. Rev. B: Condens. Matter Mater. Phys.* **1972**, 6 (12), 4370−4379.

(17) Jiao, X.; Goeckeritz, J.; Blair, S.; Oldham, M. Localization of Near-Field Resonances in Bowtie Antennae: Influence of Adhesion Layers. *Plasmonics* **2009**, 4 (1), 37−50.

(18) Knight, M. W.; Halas, N. J. Nanoshells to nanoeggs to nanocups: optical properties of reduced symmetry core−shell nanoparticles beyond the quasistatic limit. *New J. Phys*. **2008**, 10 (10), 105006.

(19) Bohren, C. F.; Huffman, D. R. Absorption and Scattering by an Arbitrary Particle. In *Absorption and Scattering of Light by Small Particles*; Wiley-VCH Verlag GmbH: Weinheim, Germany, 1998; pp 71−72.

(20) Ding, W.; Bachelot, R.; Kostcheev, S.; Royer, P.; Espiau de Lamaestre, R. Surface plasmon resonances in silver Bowtie nanoantennas with varied bow angles. *J. Appl. Phys.* **2010**, 108 (12), 124314−1−6.

(21) Fromm, D. P.; Sundaramurthy, A.; Schuck, P. J.; Kino, G.; Moerner, W. E. Gap-Dependent Optical Coupling of Single "Bowtie" Nanoantennas Resonant in the Visible. *Nano Lett.* **2004**, 4 (5), 957−961.

(22) Goebl, J.; Zhang, Q.; He, L.; Yin, Y. Monitoring the Shape Evolution of Silver Nanoplates: A Marker Study. *Angew. Chem., Int. Ed.* **2012**, 51 (2), 552−555.

3. Nanocube Metasurfaces Displaying Extreme Light Confinement in the Infrared

3.1 Introduction

Metasurfaces are ultrathin, two-dimensional arrays of subwavelength resonators that have been demonstrated to control the flow of light in ways that are otherwise unattainable with natural materials.[1-4] For operation in the optical to near-infrared (IR) range, these arrays are typically composed of metallic Ag or Au nanostructures shaped like split-rings,[5] nanowire pairs,[6] or nanorods.[7] Individually, these nanostructures operate by supporting the excitation of localized or propagating surface plasmons: Localized surface plasmon resonances (LSPRs) are generated when light impinging on a nanostructured metal surface couples to the free electrons in the metal. LSPR excitation produces highly localized light confinement, with an evanescent field that extends tens of nanometers beyond the metal surface. Surface plasmon polaritons (SPPs) are propagating electromagnetic waves that are bound to a metal-dielectric interface. SPPs can propagate for tens of microns in-plane, but decay evanescently out-of-plane. In a metasurface, these nanostructures (also referred to as meta-atoms) are arranged such that they experience inductive or capacitive coupling, giving rise to a collective electromagnetic response. In general, changing the size and shape of the individual metallic nanostructures tunes the permittivity, $\varepsilon(\omega)$, while changing the arrangement and spacing of the overall array tunes the permeability, $\mu(\omega)$, of the metasurface. In this manner, the electromagnetic response

of the metasurface can be tuned within the optical and terahertz frequency ranges and can produce effects such as narrow- and broad-band tailoring of material absorption and reflection,[8] graded birefringence for light steering,[9] and total phase control.[10]

One of the biggest challenges in utilizing metasurfaces for these applications is the ability to fabricate these materials over large areas. Lithographic methods are capable of fabricating meta-atoms, with the ability to produce metallic nanostructures with adequate uniformity within micrometer-sized arrays.[11] However, fabricating these nanostructures over larger areas becomes prohibitively expensive and time-consuming. To overcome this fabrication challenge, bottom-up methods for producing metasurfaces are highly desirable. Colloidal nanocrystals have been demonstrated as nanoscale building blocks for the assembly of large-area plasmonic metamaterials[12,13,14] Shaped nanocrystals can be arranged into 2-D arrays using bench-top techniques such as self-assembly, polymer-mediated assembly, solvent-casting, and spin-coating.[15] These approaches are advantageous for constructing metasurfaces due to their scalability and ease of fabrication. In demonstration of such an approach, Moreau and co-workers recently fabricated a metasurface composed of colloidal Ag nanocubes deposited onto an Au thin-film.[16] Coupling between individual Ag nanocubes and the underlying Au film produced a highly absorbing metasurface whose resonant wavelength is tuned by controlling the out-of-plane dielectric spacing between these two components. Significantly, this work established that colloidal nanoparticles can serve as appropriate meta-atoms for metasurfaces that operate in the visible wavelength range.

To achieve metasurface operation at longer wavelengths out into the infrared, colloidal nanoparticles that exhibit LSPRs beyond the visible wavelengths can be chosen. Alternatively, another approach to extend the operational wavelength range of a metasurface is to utilize the effect of in-plane electromagnetic coupling between individual resonators. Typically, when metallic nanoparticles are placed in close proximity of each other, inductive or capacitive coupling can occur to give rise to a collective electromagnetic response.[17] In-plane coupling is expected to provide an additional design variable for colloidal metasurfaces. In the case of Ag nanocubes on a metal film (which we abbreviate here as NOM metasurfaces), Moreau and colleagues examined arrays with low nanoparticle surface coverages between 4-17%. The nanocubes in their arrays possess interparticle spacings in the range of 190-350 nm, where interactions between neighboring nanocubes are negligible.[18] Based on our previous work with Ag nanocubes and their self-assembly,[19] we expect that closely-spaced nanocubes with interparticle spacings in the range of 1-100 nm should give tunable reflectance and absorbance properties over longer wavelength ranges.

3.2 Methodology

Simulation

We carried out two-dimensional electrodynamic simulations using a commercial finite difference time domain (FDTD) software package (Lumerical). The majority of the simulations were run on the San Diego Super Computer Center's Triton Shared Computing Cluster (TSCC). Simulation times ranged from 10 minutes to 12 hours depending on the size of the structure being evaluated. Refractive index data for Ag was interpolated from

Palik.[20] In all simulations, the metasurface was modeled in an air (n=1) environment, and light propagation is taken in the y-direction (perpendicular to substrate).

Simulations were performed for incident light with wavelengths between 250-4250 nm and electric field strengths of 1 V/m at standard temperature and pressure. Initial simulations were run with a step size of approximately 20 nm; to achieve better spectral resolution near the LSPR wavelength, additional simulations were run with a step size of 1.3 nm. The initial electric field before the addition of light was set at 0 V/m. For most simulations the FDTD solution box was approximately 300 nm wide and 1500 nm high. Periodic boundary conditions were used in the x dimension in order to simulate an infinite film. In the y direction perfectly matched layer (PML) boundary conditions were used. A mesh accuracy of 8 with an additional mesh of 0.5 nm in both the x and y being added in area of the geometry. A Total-Field Scattered-Field (TFSF) source was added to inject a plane wave of light with the propagation direction perpendicular to the substrate (y) and the polarization parallel to the substrate (x). Analysis groups that monitor the total and scattered light were added with the “total” being place inside of the source and the “scat” being place outside the source. These analysis group were obtained from the Lumerical website’s silver nanowire model. They are used for the calculation of the extinction, scattering, and absorption cross-sections of the simulation. A frequency-domain field profile monitor was added to collection the 2D color maps of the electric and magnetic fields. These were set to specifically collect data near or at the various modes of the metasurface.

The data collection and analysis was done using a series of scripts written using the Lumerical scripting language and MATLAB. See Appendix A for included scripts. One post processing of the data that is worth noting is the use of bilinear interpolation in order to in prove the quality of the image by reducing pixel size and increasing the number pixels.

3.3 Results and Discussion

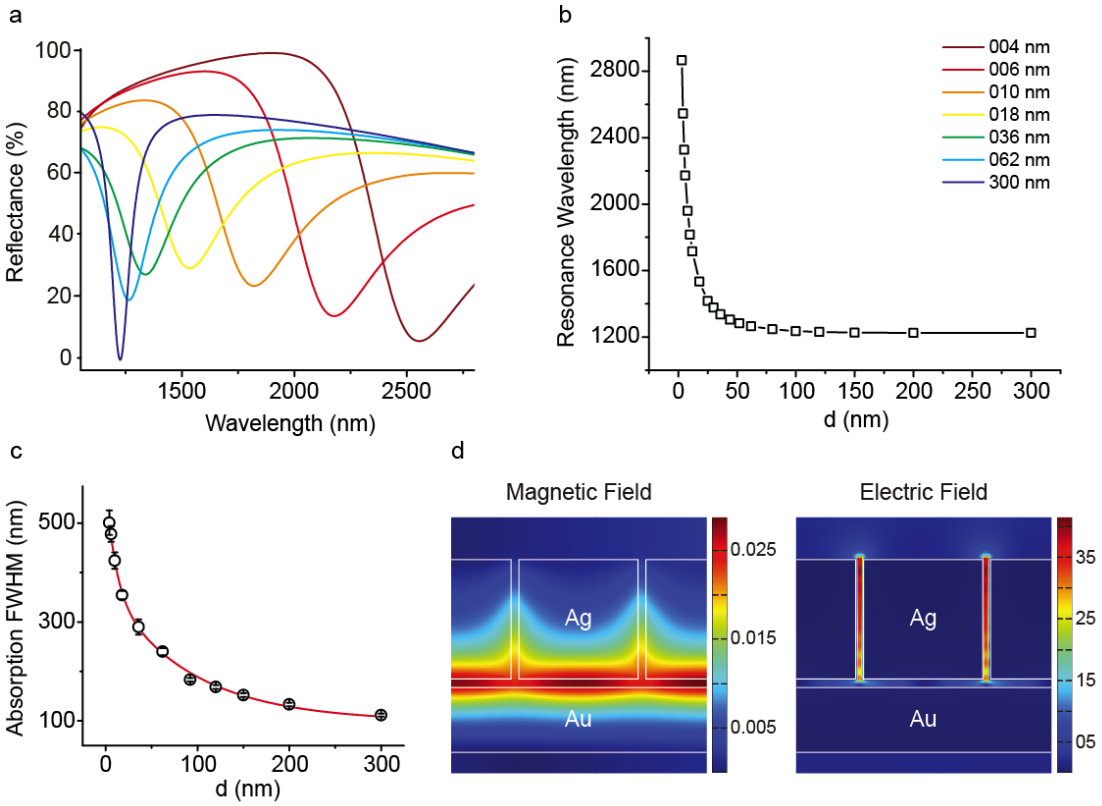

Figure 3.1 | FDTD simulations of NOM metasurfaces with varying interparticle spacing. (a) Reflectance spectra of simulated NOM arrays of 92 nm Ag nanocubes with d=4-300 nm. (b) Plot showing exponential trend of fundamental resonance wavelength as a function of interparticle spacing. (c) Various values of the FWHM of the fundamental resonance in the absorption spectra, showing the increase in spectral linewidth for decreasing d.(d) Magnetic and electric field moduli for a close-packed NOM metasurface. For d=4 nm, the fundamental resonance (shown) lies at 2544 nm. The high-field regions (red) for the H-field are supported below the nanocube; whereas for E-field are supported in the inter-nanocube gap.

Figure 3.1a shows finite-difference time-domain (FDTD) simulations of the optical response for NOM structures composed of 92-nm Ag nanocubes that possess different interparticle spacings between d=4-300 nm. The fundamental mode, which is defined as the lowest-order resonance of the metasurface, is exhibited by a sharp decrease in the reflectance spectra corresponding to near-perfect absorption. Figure 3.1b is a plot of the resonant wavelength of the fundamental mode as a function of d, showing an exponential decrease in wavelength as d is increased. This relationship that has been well-observed for plasmonic nanoparticle pairs,[20] clusters,[21] and arrays.[22] For nanocubes spaced with d=3 nm, nanocubes experience strong electromagnetic coupling and the fundamental mode is centered at λ=2865 nm. As d is increased, this value approaches the resonance wavelength reported for randomly dispersed nanocubes, with λ=1225 nm for d=300 nm. These large interparticle spacings present meta-atoms in the weak coupling limit.

As d is increased, we observe that the linewidth of the fundamental mode sharpens significantly, from 500.83±24.95 nm for d=4 nm to 111.49±2.97 nm for d=300 nm. (Figure 3.1c) This is opposite to the effect observed for nanoparticle pairs, where radiation dampening decreases when interparticle spacing is < 20 nm and the linewidth decreases to less than 50% of the linewidth observed for isolated particles.[23] This can be explained by considering how the SPPs propagating at the Au thin-film surface interact with the fundamental mode volume for isolated versus coupled nanocubes in the NOM structure. Because the thickness of the Au thin-film is close to the optical skin depth of Au, the SPPs bound to each individual metal-dielectric interface couples, resulting in a single slow-SPP mode.[24] Compared to SPPs at a bulk metal-dielectric interface which are close to free

propagating light waves, the slow-SPPs have significantly increased propagation loss, allowing for nanoscale field localization.

Figure 3.1d shows the simulated magnetic and electric field current densities for the fundamental mode at λ=2544 that give rise to the strong absorbance observed for the close-packed nanocube spacing of *d*=4 nm in Figure 3.1a. The resonance supported by the nanocube-film cavity, or gap-plasmon mode, displays interferometric effects similar to a Fabry-Perot resonator.[16] The Ag nanocubes act as waveguides, focusing slow-SPPs into the nanometer-size cavity created in-between each nanocube and the underlying Au thin-film, producing multiple reflections of the gap-plasmon mode at the nanocube edges. Constructive interference caused by reflections of the gap-mode within the cavity generates standing waves at gap resonances, resulting in almost all of the incident energy being dissipated into the metasurface.[25] The number of standing waves, or antinodes supported by the cavity determines the quality of the absorption. The fundamental resonance displays a single out-of-plane magnetic field antinode, localized to the nanocube-Au film gap. The dipolar oscillations excited in the nanocube drives anti-symmetric oscillations in the underlying Au thin-film, giving rise to a "magnetic resonance".[26] The close-packed nanocube film effectively combines the localized magnetic cavity resonances, resulting in a quasi-continuous magnetic gap-plasmon mode across the entire metasurface (figure 3.1d). An electric field node is located in the region of greatest intensity for the corresponding magnetic field. For isolated nanocubes, the local field is highly confined to the dielectric space between one cube and the underlying Au film. Increasing inter-

nanocube coupling results in the local field volume spreading to the interstitial spaces between nanocubes, which increases the mode volume by nearly five times.

Chapter 3, in part is a reprint of material that is being prepared for submission. Rozin, Matthew, Rosen, David, Tao, Andrea. The Thesis author was the secondary investigator of this material.

3.5 Appendix A

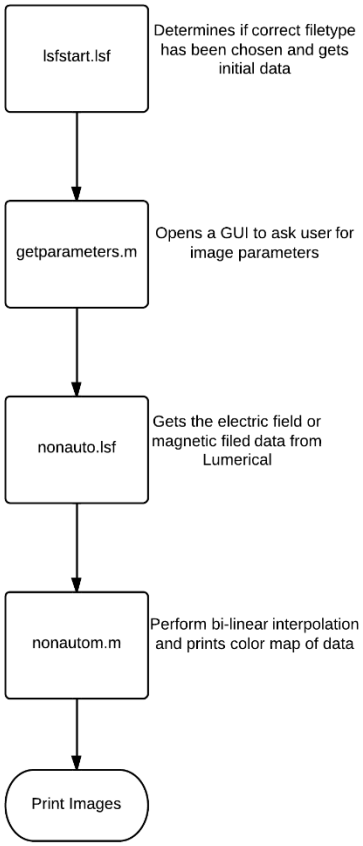

Scheme 3.1. Flowchart for the Lumerical and MATLAB scripts used to generate 2D electric and magnetic field images. The user first runs lsfstart.lsf and chooses the lumerical file that the images are to be gotten from. The script then proceeds to open the graphical user interface (GUI) and then generate images based on the selected options.

3.6.1 lsfstart.lsf

```
#Script to gather initial parameters
clear;

#add script paths
#matlab("addpath('/home/drosen/scripts/')");
matlab("addpath('/home/drosen/scripts/matlabscripts')");
addpath("/home/drosen/scripts/lsfscripts/");
addpath("/home/drosen/scripts/matlabscripts/");


#get file name and path
fsppath = currentfilename;          #no / at end, has .fsp at end
jobpath = filedirectory(fsppath);   #no / at end
fspname = filebasename(fsppath);    #no / or .fsp at end

#check if run in batch mode
if (fsppath == "") {
        ?endl + "No fsp file selected running in batch mode." + endl;
        batchlsf;
#       exit;
}

matlabput(fspname,fsppath,jobpath);

#get monitor names
mNames = splitstring(getresult,endl);
matlabput(mNames);

matlab("monitor = {};
    for i=1:length(mNames)
                    if(strfind(mNames{i},'monitor') == 1)
                            monitor{end+1} = mNames{i};
                end
        end
");

matlabget(monitor);

#get wavelength/efield/hfield range

wamax = 1:length(monitor);
wmin = 1:length(monitor);
emax = 1:length(monitor);
emin = 1:length(monitor);
hmax = 1:length(monitor);
hmin = 1:length(monitor);

for (i=1:length(monitor)) {
        E = getresult(monitor{i},"E");
        H = getresult(monitor{i},"H");
        wamax(i) = round(c/min(E.f) * 1e9);
```

```
		wmin(i) = round(c/max(E.f) * 1e9);

		emax(i) = max(sqrt(E.E2));
		emin(i) = min(sqrt(E.E2));

		hmax(i) = max(sqrt(H.H2));
		hmin(i) = min(sqrt(H.H2));
}

matlabput(wamax,wmin,emax,emin,hmax,hmin);

#Get parameters from user
matlab("getparameters");
matlabget(Answer, Cancelled);

if(Cancelled == 1) {
		exit;
}

#If allauto was checked
if(Answer.allauto == 1) {
		allautolsf;
		exit;
}

#Make appropriate directories

matlab("if exist(strcat(jobpath,'/',fspname,'_plots')) ~= 7
				mkdir(strcat(jobpath,'/',fspname,'_plots'));
			end

			for i=1:length(monitor)
				if Answer.(strcat('eplot_',monitor{i})) == 1 && Answer.(monitor{i}) == 1 &&
Answer.(strcat('scale_',monitor{i})) == 1
					if exist(strcat(jobpath,'/',fspname,'_plots','/',fspname,'_EFplots')) ~=7

		mkdir(strcat(jobpath,'/',fspname,'_plots','/',fspname,'_EFplots'));
					end
					if
exist(strcat(jobpath,'/',fspname,'_plots','/',fspname,'_EFplots','/',monitor{i})) ~=7

		mkdir(strcat(jobpath,'/',fspname,'_plots','/',fspname,'_EFplots','/',monitor{i}));
					end
				end

				if Answer.(strcat('hplot_',monitor{i})) == 1 && Answer.(monitor{i}) == 1 &&
Answer.(strcat('scale_',monitor{i})) == 1
					if exist(strcat(jobpath,'/',fspname,'_plots','/',fspname,'_HFplots')) ~=7

		mkdir(strcat(jobpath,'/',fspname,'_plots','/',fspname,'_HFplots'));
					end
					if
exist(strcat(jobpath,'/',fspname,'_plots','/',fspname,'_HFplots','/',monitor{i})) ~=7
```

```
        mkdir(strcat(jobpath,'/',fspname,'_plots','/',fspname,'_HFplots','/',monitor{i}));
                                    end
                                end

                                if Answer.(strcat('evect_',monitor{i})) == 1 && Answer.(monitor{i}) == 1 &&
Answer.(strcat('scale_',monitor{i})) == 1
                                    if exist(strcat(jobpath,'/',fspname,'_plots','/',fspname,'_EFvectors')) ~=7

        mkdir(strcat(jobpath,'/',fspname,'_plots','/',fspname,'_EFvectors'));
                                    end
                                    if
exist(strcat(jobpath,'/',fspname,'_plots','/',fspname,'_EFvectors','/',monitor{i})) ~=7

        mkdir(strcat(jobpath,'/',fspname,'_plots','/',fspname,'_EFvectors','/',monitor{i}));
                                    end
                                end

                                if Answer.(strcat('hvect_',monitor{i})) == 1 && Answer.(monitor{i}) == 1 &&
Answer.(strcat('scale_',monitor{i})) == 1
                                    if exist(strcat(jobpath,'/',fspname,'_plots','/',fspname,'_HFvectors')) ~=7

        mkdir(strcat(jobpath,'/',fspname,'_plots','/',fspname,'_HFvectors'));
                                    end
                                    if
exist(strcat(jobpath,'/',fspname,'_plots','/',fspname,'_HFvectors','/',monitor{i})) ~=7

        mkdir(strcat(jobpath,'/',fspname,'_plots','/',fspname,'_HFvectors','/',monitor{i}));
                                    end
                                end

                                if Answer.(strcat('eplot_',monitor{i})) == 1 && Answer.(monitor{i}) == 1 &&
Answer.(strcat('grid_',monitor{i})) == 1
                                    if     exist(strcat(jobpath,'/',fspname,'_plots','/',fspname,'_EFplots_grid'))
~=7

        mkdir(strcat(jobpath,'/',fspname,'_plots','/',fspname,'_EFplots_grid'));
                                    end
                                    if
exist(strcat(jobpath,'/',fspname,'_plots','/',fspname,'_EFplots_grid','/',monitor{i})) ~=7

        mkdir(strcat(jobpath,'/',fspname,'_plots','/',fspname,'_EFplots_grid','/',monitor{i}));
                                    end
                                end

                                if Answer.(strcat('hplot_',monitor{i})) == 1 && Answer.(monitor{i}) == 1 &&
Answer.(strcat('grid_',monitor{i})) == 1
                                    if     exist(strcat(jobpath,'/',fspname,'_plots','/',fspname,'_HFplots_grid'))
~=7

        mkdir(strcat(jobpath,'/',fspname,'_plots','/',fspname,'_HFplots_grid'));
                                    end
```

```
                                        if
exist(strcat(jobpath,'/',fspname,'_plots','/',fspname,'_HFplots_grid','/',monitor{i})) ~=7

        mkdir(strcat(jobpath,'/',fspname,'_plots','/',fspname,'_HFplots_grid','/',monitor{i}));
                                        end
                                end

                                if Answer.(strcat('evect_',monitor{i})) == 1 && Answer.(monitor{i}) == 1 &&
Answer.(strcat('grid_',monitor{i})) == 1
                                        if exist(strcat(jobpath,'/',fspname,'_plots','/',fspname,'_EFvectors_grid'))
~=7

        mkdir(strcat(jobpath,'/',fspname,'_plots','/',fspname,'_EFvectors_grid'));
                                        end
                                        if
exist(strcat(jobpath,'/',fspname,'_plots','/',fspname,'_EFvectors_grid','/',monitor{i})) ~=7

        mkdir(strcat(jobpath,'/',fspname,'_plots','/',fspname,'_EFvectors_grid','/',monitor{i}));
                                        end
                                end

                                if Answer.(strcat('hvect_',monitor{i})) == 1 && Answer.(monitor{i}) == 1 &&
Answer.(strcat('grid_',monitor{i})) == 1
                                        if exist(strcat(jobpath,'/',fspname,'_plots','/',fspname,'_HFvectors_grid'))
~=7

        mkdir(strcat(jobpath,'/',fspname,'_plots','/',fspname,'_HFvectors_grid'));
                                        end
                                        if
exist(strcat(jobpath,'/',fspname,'_plots','/',fspname,'_HFvectors_grid','/',monitor{i})) ~=7

        mkdir(strcat(jobpath,'/',fspname,'_plots','/',fspname,'_HFvectors_grid','/',monitor{i}));
                                        end
                                end
                        end
        ');

if(Answer.allauto ~= 1) {
        nonauto;
}
```

3.6.2 getparameters.m

```
close all;

Options.Resize = 'on';
Options.Interpreter = 'tex';
Options.CancelButton = 'on';
Options.ApplyButton = 'off';
Options.ButtonNames = {'OK','Cancel'};
Options.AlignControls = 'on';
```

```
Title = 'Input Parameters';

Prompt = {};
Formats = {};
DefAns = struct([]);
wmax = [];


Prompt(1,:) = {'Auto All','allauto',[]};
Formats(1,1).type = 'check';

Prompt(end+1,:) = {'Generate Spectra?','spectra',[]};
Formats(1,2).type = 'check';
Formats(1,2).labelloc = 'topcenter';
DefAns(1).spectra = true;


Prompt(end+1,:) = {'  Smoothing scale factor:','smoothing',[]};
Formats(1,3).type = 'edit';
Formats(1,3).size = [40 30];
Formats(1,3).format = 'integer';
DefAns.smoothing = 10;

Prompt(end+1,:) = {'Monitor Names:',[],[]};
Formats(2,1).type = 'text';

for i=1:length(monitor)
    Prompt(end+1,:) = {monitor{i},monitor{i},[]};
    Formats(2,i*2).type = 'check';

    Prompt(end+1,:) = {' ',[],[]};
    Formats(2,2*i+1).type = 'text';
end



Prompt(end+1,:) = {'Wavelength range:',[],[]};
Formats(3,1).type = 'text';

for i=1:length(monitor)
   Prompt(end+1,:) = {'  min:',strcat('wmin_',monitor{i}),'nm'};
   Formats(3,2*i).type = 'edit';
   Formats(3,2*i).size = [40 30];
   Formats(3,2*i).unitsloc = 'rightmiddle';
   Formats(3,2*i).labelloc = 'topcenter';
   Formats(3,2*i).format = 'float';
   DefAns.(strcat('wmin_',monitor{i})) = wmin(i);

   Prompt(end+1,:) = {'  max:',strcat('wmax_',monitor{i}),'nm'};
   Formats(3,2*i+1).type = 'edit';
   Formats(3,2*i+1).size = [40 30];
   Formats(3,2*i+1).unitsloc = 'rightmiddle';
   Formats(3,2*i+1).labelloc = 'topcenter';
```

```
    Formats(3,2*i+1).format = 'float';
    DefAns.(strcat('wmax_',monitor{i})) = wamax(i);
end

Prompt(end+1,:) = {'E-Field colorbar range:',[],[]};
Formats(4,1).type = 'text';

for i=1:length(monitor)
    Prompt(end+1,:) = {'  min:',strcat('cemin_',monitor{i}),[]};
    Formats(4,2*i).type = 'edit';
    Formats(4,2*i).size = [40 30];
    Formats(4,2*i).labelloc = 'topcenter';
    Formats(4,2*i).format = 'float';
    DefAns.(strcat('cemin_',monitor{i})) = emin(i);

    Prompt(end+1,:) = {'  max:',strcat('cemax_',monitor{i}),[]};
    Formats(4,2*i+1).type = 'edit';
    Formats(4,2*i+1).size = [40 30];
    Formats(4,2*i+1).labelloc = 'topcenter';
    Formats(4,2*i+1).format = 'float';
    DefAns.(strcat('cemax_',monitor{i})) = emax(i);
end

Prompt(end+1,:) = {'H-Field colorbar range:',[],[]};
Formats(5,1).type = 'text';

for i=1:length(monitor)
    Prompt(end+1,:) = {'  min:',strcat('chmin_',monitor{i}),[]};
    Formats(5,2*i).type = 'edit';
    Formats(5,2*i).size = [40 30];
    Formats(5,2*i).labelloc = 'topcenter';
    Formats(5,2*i).format = 'float';
    DefAns.(strcat('chmin_',monitor{i})) = hmin(i);

    Prompt(end+1,:) = {'  max:',strcat('chmax_',monitor{i}),[]};
    Formats(5,2*i+1).type = 'edit';
    Formats(5,2*i+1).size = [40 30];
    Formats(5,2*i+1).labelloc = 'topcenter';
    Formats(5,2*i+1).format = 'float';
    DefAns.(strcat('chmax_',monitor{i})) = hmax(i);
end

Prompt(end+1,:) = {'Choose plots:',[],[]};
Formats(6,1).type = 'text';

for i=1:length(monitor)
    Prompt(end+1,:) = {'  E-Field',strcat('eplot_',monitor{i}),[]};
    Formats(6,2*i).type = 'check';
    Formats(6,2*i).labelloc = 'topcenter';

    Prompt(end+1,:) = {'  H-Field',strcat('hplot_',monitor{i}),[]};
    Formats(6,2*i+1).type = 'check';
    Formats(6,2*i+1).labelloc = 'topcenter';
```

```
end

for i=1:length(monitor)
   Prompt(end+1,:) = {'  E-Field Vector',strcat('evect_',monitor{i}),[]};
   Formats(7,2*i).type = 'check';
   Formats(7,2*i).labelloc = 'topcenter';

   Prompt(end+1,:) = {'  H-Field Vector',strcat('hvect_',monitor{i}),[]};
   Formats(7,2*i+1).type = 'check';
   Formats(7,2*i+1).labelloc = 'topcenter';
end

Prompt(end+1,:) = {'Data points per vector',[],[]};
Formats(8,1).type = 'text';

Prompt(end+1,:) = {'  ', 'vpoints',[]};
Formats(8,2).type = 'edit';
Formats(8,2).size = [40 30];
Formats(8,2).format = 'integer';
DefAns.vpoints = 2;

Prompt(end+1,:) = {'Grid or Scalebar',[],[]};
Formats(9,1).type = 'text';

for i=1:length(monitor)
   Prompt(end+1,:) = {'  Scalebar',strcat('scale_',monitor{i}),[]};
   Formats(9,2*i).type = 'check';
   Formats(9,2*i).labelloc = 'topcenter';
   DefAns.(strcat('scale_',monitor{i})) = true;

   Prompt(end+1,:) = {'  Grid',strcat('grid_',monitor{i}),[]};
   Formats(9,2*i+1).type = 'check';
   Formats(9,2*i+1).labelloc = 'topcenter';
end

[Answer,Cancelled] = inputsdlg(Prompt,Title,Formats,DefAns,Options); %inputsdlg from matlabcentral
Copyright (c) 2013, Takeshi Ikuma

%Collects selected options and converts to double for Lumerical
Answer.allauto = +Answer.allauto;
Answer.spectra = +Answer.spectra;
Cancelled = +Cancelled;

for i=1:length(monitor)
   Answer.(monitor{i}) = +Answer.(monitor{i});
   Answer.(strcat('wmin_',monitor{i})) = +Answer.(strcat('wmin_',monitor{i}));
   Answer.(strcat('wmax_',monitor{i})) = +Answer.(strcat('wmax_',monitor{i}));
   Answer.(strcat('cemin_',monitor{i})) = +Answer.(strcat('cemin_',monitor{i}));
   Answer.(strcat('cemax_',monitor{i})) = +Answer.(strcat('cemax_',monitor{i}));
   Answer.(strcat('chmin_',monitor{i})) = +Answer.(strcat('chmin_',monitor{i}));
   Answer.(strcat('chmax_',monitor{i})) = +Answer.(strcat('chmax_',monitor{i}));
   Answer.(strcat('eplot_',monitor{i})) = +Answer.(strcat('eplot_',monitor{i}));
   Answer.(strcat('hplot_',monitor{i})) = +Answer.(strcat('hplot_',monitor{i}));
```

```
   Answer.(strcat('evect_',monitor{i})) = +Answer.(strcat('evect_',monitor{i}));
   Answer.(strcat('hvect_',monitor{i})) = +Answer.(strcat('hvect_',monitor{i}));
   Answer.(strcat('scale_',monitor{i})) = +Answer.(strcat('scale_',monitor{i}));
   Answer.(strcat('grid_',monitor{i})) = +Answer.(strcat('grid_',monitor{i}));
end
```

3.6.3 nonauto.lsf

```
#This script runs if allauto box was not checked in getparameters.
#It will take the info from getparameters and gather the appropiate
#data from the model.

matlab("addpath('/home/drosen/scripts/matlabscripts')");
addpath("/home/drosen/scripts/lsfscripts/");
addpath("/home/drosen/scripts/matlabscripts/");

#check which monitors and plots were selected.

matlab("
                selected_mons = [];
                wavlength_min = [];
                wavlength_max = [];

                for i=1:length(monitor)
                                selected_mons(i) = Answer.(monitor{i});
                                wavlength_min(i) = Answer.(strcat('wmin_',monitor{i}));
                                wavlength_max(i) = Answer.(strcat('wmax_',monitor{i}));

                end
        ");

matlabget(selected_mons,wavlength_min,wavlength_max);

if (Answer.spectra == 1) {
        ?'Generating Spectra (ignore the next line)';
        spectra;
}


#Get results from selected monitors
for (i=1:length(monitor)) {
        if (haveresult(monitor{i},"E")) {
                if (selected_mons(i) == 1) {
                                E = getresult(monitor{i},"E");
                                Ex = E.x * 1e9;
                                Ey = E.y * 1e9;

                                f = E.f;
                                f_points = size(E.f);

                                H = getresult(monitor{i},"H");
                                Hx = H.x * 1e9;
```

```
                Hy = H.y * 1e9;

            for (n=1; n<=f_points; n=n+1) {
                fn = f(n);
                wavelength = round(c/fn*1e9);

                if (wavelength >= wavlength_min(i)) {
                    if (wavelength <= wavlength_max(i)) {
                        Eint = pinch(sqrt(E.E2),4,n);
                        Hint = pinch(sqrt(H.H2),4,n);

                        EFx = pinch(E.Ex,4,n);
                        EFy = pinch(E.Ey,4,n);
                        HFx = pinch(H.Hx,4,n);
                        HFy = pinch(H.Hy,4,n);


    matlabput(Ex,Ey,Hx,Hy,Eint,Hint,EFx,EFy,HFx,HFy,fn,i,n);
                        ?'Printing images for ' + num2str(wavelength) + ' nm';

                        matlab("nonautom;");
                    }
                }
            }
        }
    }
}
```

3.6.4 nonauto.m

```
% Matlab companion to nonauto.lsf
% This Script will run for each datapoint.

c = 299792458;
wavelength = c/fn * 1e9;
wavelengthstr = num2str(round(wavelength));
filename = strcat(fspname,'_',monitor{i},'_',wavelengthstr,'nm');
addpath('/home/drosen/scripts/matlabscripts');

EFx = EFx .* conj(EFx);
EFy = EFy .* conj(EFy);
HFx = HFx .* conj(HFx);
HFy = HFy .* conj(HFy);

Eint = rot90(Eint,3);
Hint = rot90(Hint,3);
EFx = rot90(EFx,3);
EFy = rot90(EFy,3);
HFx = rot90(HFx,3);
HFy = rot90(HFy,3);

Ex2 = Ex(1:Answer.vpoints:end,1:Answer.vpoints:end);
```

```
Ey2 = Ey(1:Answer.vpoints:end,1:Answer.vpoints:end);
EFx2 = EFx(1:Answer.vpoints:end,1:Answer.vpoints:end);
EFy2 = EFy(1:Answer.vpoints:end,1:Answer.vpoints:end);
Hx2 = Hx(1:Answer.vpoints:end,1:Answer.vpoints:end);
Hy2 = Hy(1:Answer.vpoints:end,1:Answer.vpoints:end);
HFx2 = HFx(1:Answer.vpoints:end,1:Answer.vpoints:end);
HFy2 = HFy(1:Answer.vpoints:end,1:Answer.vpoints:end);

Eintfiltered = imresize(Eint,Answer.smoothing,'bilinear');
Hintfiltered = imresize(Hint,Answer.smoothing,'bilinear');

remax = round(emax(i)*1000)/1000;
remin = round(emin(i)*1000)/1000;
rcemax = round(Answer.(strcat('cemax_',monitor{i}))*1000)/1000;
rcemin = round(Answer.(strcat('cemin_',monitor{i}))*1000)/1000;

cemax = Answer.(strcat('cemax_',monitor{i}));
cemin = Answer.(strcat('cemin_',monitor{i}));

rhmax = round(hmax(i)*1000)/1000;
rhmin = round(hmin(i)*1000)/1000;

chmax = Answer.(strcat('chmax_',monitor{i}));
chmin = Answer.(strcat('chmin_',monitor{i}));

rchmax = round(Answer.(strcat('chmax_',monitor{i}))*1000)/1000;
rchmin = round(Answer.(strcat('chmin_',monitor{i}))*1000)/1000;

if Answer.(strcat('scale_',monitor{i})) == 1
        if Answer.(strcat('eplot_',monitor{i})) == 1
                %Print Efield plots
                fig = figure('Units','Pixels','visible', 'off','Resize','off');
                        imagesc(Ex,Ey,Eintfiltered);
                                colormap(jet(4096));
                    axis image;
                    colorbar;

                    if (abs(emax-cemax)/emax < .1) && (abs(emin-cemin)/emin < .1)

                        caxis('auto');
                                else
                                        caxis([Answer.(strcat('cemin_',monitor{i})),
Answer.(strcat('cemax_',monitor{i}))]);
                                end

                            set(gca,'visible','off');
                            set(gcf, 'Renderer', 'Zbuffer');
                    scalebar('color',[.9 .9 .9],'bold','true','location','southeast','scalelength',25); %scalebar
from matlabcentral Copyright © 2009, Amanda Ng
                            print('-dpng',
strcat(jobpath,'/',fspname,'_plots','/',fspname,'_EFplots','/',monitor{i},'/',filename,'_E'), '-r100');
                close all;
        end
```

```
        if Answer.(strcat('hplot_',monitor{i})) == 1
                %Print Hfield plots
                fig = figure('Units','Pixels','visible', 'off','Resize','off');
                        imagesc(Hx,Hy,Hintfiltered);
                                colormap(jet(4096));
                    axis image;
                    colorbar;


                                if (abs(hmax-chmax)/hmax < .1) && (abs(hmin-chmin)/hmin < .1)

                        caxis('auto');
                                else
                                        caxis([Answer.(strcat('chmin_',monitor{i})),
Answer.(strcat('chmax_',monitor{i}))]);
                                end

                           set(gca,'visible','off');
                           set(gcf, 'Renderer', 'Zbuffer');
                    scalebar('color',[.9 .9 .9],'bold','true','location','southeast','scalelength',25);
                        print('-dpng',
strcat(jobpath,'/',fspname,'_plots','/',fspname,'_HFplots','/',monitor{i},'/',filename,'_H'), '-r100');
                close all;
        end

        if Answer.(strcat('evect_',monitor{i})) == 1
                %Print Efield vectors
                fig = figure('Units','Pixels','visible', 'off','Resize','on');
                        imagesc(Ex,Ey,Eintfiltered);
                        hold on
                        %scale = .5;
                        quiver(Ex2,Ey2,EFx2,EFy2,'color',[0 0 0]);
                        %quiver(Ex,Ey,EFx,EFy,'color',[.5 .5 .5]);

                                colormap(jet(4096));
                    axis image;
                    colorbar;

                    if (abs(emax-cemax)/emax < .1) && (abs(emin-cemin)/emin < .1)

                        caxis('auto');
                                else
                                        caxis([Answer.(strcat('cemin_',monitor{i})),
Answer.(strcat('cemax_',monitor{i}))]);
                                end

                           set(gca,'visible','off');
                           set(gcf, 'Renderer', 'Zbuffer');
                    scalebar('color',[.9 .9 .9],'bold','true','location','southeast','scalelength',25);

saveas(fig,strcat(jobpath,'/',fspname,'_plots','/',fspname,'_EFvectors','/',monitor{i},'/',filename,'_vectors_E'),'
fig');
```

```
makevisible(strcat(jobpath,'/',fspname,'_plots','/',fspname,'_EFvectors','/',monitor{i},'/',filename,'_vectors_E
.fig'));
                close all;
        end

        if Answer.(strcat('hvect_',monitor{i})) == 1
                %Print Hfield vectors
                fig = figure('Units','Pixels','visible', 'off','Resize','on');
                        imagesc(Hx,Hy,Hintfiltered);
                                        hold on
                        quiver(Hx2,Hy2,HFx2,HFy2,'color',[0 0 0]);
                                colormap(jet(4096));
                    axis image;
                    colorbar;

                                if (abs(hmax-chmax)/hmax < .1) && (abs(hmin-chmin)/hmin < .1)

                    caxis('auto');
                                else
                                        caxis([Answer.(strcat('chmin_',monitor{i})),
Answer.(strcat('chmax_',monitor{i}))]);
                                end

                                  set(gca,'visible','off');
                                  set(gcf, 'Renderer', 'Zbuffer');
                    scalebar('color',[.9 .9 .9],'bold','true','location','southeast','scalelength',25);

saveas(fig,strcat(jobpath,'/',fspname,'_plots','/',fspname,'_HFvectors','/',monitor{i},'/',filename,'_vectors_H'),
'fig');

makevisible(strcat(jobpath,'/',fspname,'_plots','/',fspname,'_HFvectors','/',monitor{i},'/',filename,'_vectors_
H.fig'));
                close all;
        end
end

%If grid selected

if Answer.(strcat('grid_',monitor{i})) == 1
        if Answer.(strcat('eplot_',monitor{i})) == 1
                %Print Efield plots
                fig = figure('Units','Pixels','visible', 'off','Resize','off');
                        imagesc(Ex,Ey,Eintfiltered);
                                colormap(jet(4096));
                    axis image;
                    colorbar;
                    xlabel('x (nm)');
                    ylabel('y (nm)');
         title(strcat({'Electric Field at: '},num2str(wavelength),{' nm'}));

                    if (abs(emax-cemax)/emax < .1) && (abs(emin-cemin)/emin < .1)
```

```
                caxis('auto');
                    else
                        caxis([Answer.(strcat('cemin_',monitor{i})),
Answer.(strcat('cemax_',monitor{i}))]);
                    end

                set(gcf, 'Renderer', 'Zbuffer');
                    set(gca,'TickDir','out');
                print('-dpng',
strcat(jobpath,'/',fspname,'_plots','/',fspname,'_EFplots_grid','/',monitor{i},'/',filename,'_E_grid'), '-r100');
            close all;
        end

        if Answer.(strcat('hplot_',monitor{i})) == 1
            %Print Hfield plots
            fig = figure('Units','Pixels','visible', 'off','Resize','off');
                imagesc(Hx,Hy,Hintfiltered);
                    colormap(jet(4096));
                axis image;
                colorbar;
                xlabel('x (nm)');
                ylabel('y (nm)');
             title(strcat({'Magnetic Field at: '},num2str(wavelength),{' nm'}));

                    if (abs(hmax-chmax)/hmax < .1) && (abs(hmin-chmin)/hmin < .1)

                caxis('auto');
                    else
                        caxis([Answer.(strcat('chmin_',monitor{i})),
Answer.(strcat('chmax_',monitor{i}))]);
                    end

                set(gcf, 'Renderer', 'Zbuffer');
                    set(gca,'TickDir','out');
                print('-dpng',
strcat(jobpath,'/',fspname,'_plots','/',fspname,'_HFplots_grid','/',monitor{i},'/',filename,'_H_grid'), '-r100');
            close all;
        end

        if Answer.(strcat('evect_',monitor{i})) == 1
            %Print Efield vectors
            fig = figure('Units','Pixels','visible', 'off','Resize','on');
                imagesc(Ex,Ey,Eintfiltered);
                        hold on
                quiver(Ex2,Ey2,EFx2,EFy2,'color',[0 0 0]);
                    colormap(jet(4096));
                axis image;
                colorbar;
                xlabel('x (nm)');
                ylabel('y (nm)');
             title(strcat({'Electric Field Vectors at: '},num2str(wavelength),{' nm'}));

                if (abs(emax-cemax)/emax < .1) && (abs(emin-cemin)/emin < .1)
```

```
                caxis('auto');
                    else
                        caxis([Answer.(strcat('cemin_',monitor{i})),
Answer.(strcat('cemax_',monitor{i}))]);
                    end

                set(gcf, 'Renderer', 'Zbuffer');
                    set(gca,'TickDir','out');

saveas(fig,strcat(jobpath,'/',fspname,'_plots','/',fspname,'_EFvectors_grid','/',monitor{i},'/',filename,'_vectors
_E_grid'),'fig');

makevisible(strcat(jobpath,'/',fspname,'_plots','/',fspname,'_EFvectors_grid','/',monitor{i},'/',filename,'_vect
ors_E_grid.fig'));
            close all;
        end

        if Answer.(strcat('hvect_',monitor{i})) == 1
            %Print Hfield vectors
            fig = figure('Units','Pixels','visible', 'off','Resize','on');
                imagesc(Hx,Hy,Hintfiltered);
                    hold on
                quiver(Hx2,Hy2,HFx2,HFy2,'color',[0 0 0]);

                    colormap(jet(4096));
                axis image;
                colorbar;
                xlabel('x (nm)');
                ylabel('y (nm)');
         title(strcat({'Magnetic Field Vectors at: '},num2str(wavelength),{' nm'}));


                    if (abs(hmax-chmax)/hmax < .1) && (abs(hmin-chmin)/hmin < .1)

                caxis('auto');
                    else
                        caxis([Answer.(strcat('chmin_',monitor{i})),
Answer.(strcat('chmax_',monitor{i}))]);
                    end

                set(gcf, 'Renderer', 'Zbuffer');
                    set(gca,'TickDir','out');

saveas(fig,strcat(jobpath,'/',fspname,'_plots','/',fspname,'_HFvectors_grid','/',monitor{i},'/',filename,'_vector
s_H_grid'),'fig');

makevisible(strcat(jobpath,'/',fspname,'_plots','/',fspname,'_HFvectors_grid','/',monitor{i},'/',filename,'_vect
ors_H_grid.fig'));
            close all;
        end
end
```

3.4 Chapter 3 References

(1) Landy, N. I.; Sajuyigbe, S.; Mock, J. J.; Smith, D. R.; Padilla, W. J., Perfect Metamaterial Absorber. *Phys. Rev. Lett.* **2008**, 100, 207402.

(2) Diem, M.; Koschny, T.; Soukoulis, C. M., Wide-angle perfect absorber/thermal emitter in the terahertz regime. *Phys. Rev. B* **2009**, 79, 033101.

(3) Avitzour, Y.; Urzhumov, Y. A.; Shvets, G., Wide-angle infrared absorber based on a negative-index plasmonic metamaterial. *Phys. Rev. B* **2009**, 79, 045131.

(4) Kildishev, A. V.; Boltasseva, A.; Shalaev, V. M., Planar Photonics with Metasurfaces. *Science* **2013**, 339.

(5) Kanté, B.; de Lustrac, A.; Lourtioz, J. M., In-plane coupling and field enhancement in infrared metamaterial surfaces. *Phy. Rev. B* 2009, 80, 035108.

(6) Dolling, G.; Enkrich, C.; Wegener, M.; Zhou, J. F.; Soukoulis, C. M.; Linden, S., Cut-wire pairs and plate pairs as magnetic atoms for optical metamaterials. *Opt. Lett.* **2005**, 30, 3198-3200.

(7) Pors, A.; Albrektsen, O.; Radko, I. P.; Bozhevolnyi, S. I., Gap plasmon-based metasurfaces for total control of reflected light. *Sci. Rep.* **2013**, 3.

(8) Bossard, J. A.; Lin, L.; Yun, S.; Liu, L.; Werner, D. H.; Mayer, T. S., Near-Ideal Optical Metamaterial Absorbers with Super-Octave Bandwidth. *ACS Nano* **2014**, 8, 1517-1524.

(9) Sun, S.; Yang, K.-Y.; Wang, C.-M.; Juan, T.-K.; Chen, W. T.; Liao, C. Y.; He, Q.; Xiao, S.; Kung, W.-T.; Guo, G.-Y.; Zhou, L.; Tsai, D. P., High-Efficiency Broadband Anomalous Reflection by Gradient Meta-Surfaces. *Nano Lett.* **2012**, 12, 6223-6229.

(10) Ni, X.; Emani, N. K.; Kildishev, A. V.; Boltasseva, A.; Shalaev, V. M., Broadband Light Bending with Plasmonic Nanoantennas. *Science* **2012**, 335, 427-427.

(11) Holloway, C. L.; Love, D. C.; Kuester, E. F.; Salandrino, A.; Engheta, N., Sub-wavelength resonators: on the use of metafilms to overcome the λ size limit. *IET microw antenna p* **2008**, 2, 120-129.

(12) Ciracì, C.; Hill, R. T.; Mock, J. J.; Urzhumov, Y.; Fernández-Domínguez, A. I.; Maier, S. A.; Pendry, J. B.; Chilkoti, A.; Smith, D. R., Probing the Ultimate Limits of Plasmonic Enhancement. *Science* **2012**, 337, 1072-1074.

(13) Mertens, J.; Eiden, A. L.; Sigle, D. O.; Huang, F.; Lombardo, A.; Sun, Z.; Sundaram, R. S.; Colli, A.; Tserkezis, C.; Aizpurua, J.; Milana, S.; Ferrari, A. C.; Baumberg, J. J., Controlling Subnanometer Gaps in Plasmonic Dimers Using Graphene. *Nano Lett.* **2013**, 13, 5033-5038.

(14) Yoshida, A.; Imazu, K.; Li, X.; Okamoto, K.; Tamada, K., Spectroscopic Properties of Multilayered Gold Nanoparticle 2D Sheets. *Langmuir* 2012, 28, 17153-17158.

(15) Konstantatos, G.; Sargent, E. H., Nanostructured materials for photon detection. *Nat. Nano.* 2010, 5, 391-400.

(16) Moreau, A.; Ciraci, C.; Mock, J. J.; Hill, R. T.; Wang, Q.; Wiley, B. J.; Chilkoti, A.; Smith, D. R., Controlled-reflectance surfaces with film-coupled colloidal nanoantennas. *Nature* **2012**, 492, 86-89.

(17) Hentschel, M.; Saliba, M.; Vogelgesang, R.; Giessen, H.; Alivisatos, A. P.; Liu, N., Transition from Isolated to Collective Modes in Plasmonic Oligomers. *Nano Lett.* **2010**, 10, 2721-2726.

(18) Liu, N.; Weiss, T.; Mesch, M.; Langguth, L.; Eigenthaler, U.; Hirscher, M.; Sönnichsen, C.; Giessen, H., Planar Metamaterial Analogue of Electromagnetically Induced Transparency for Plasmonic Sensing. *Nano Lett.* **2009**, 10, 1103-1107.

(19) Gao, B.; Arya, G.; Tao, A. R. Self-Orienting Nanocubes for the Assembly of Plasmonic Nanojunctions. *Nat Nano* **2012**, *7*, 433–437.

(20) Palik, E. D.; Ghosh, G. Handbook of Optical Constants of Solids, 1998, 5 v.

(21) Atay, T.; Song, J.-H.; Nurmikko, A. V., Strongly Interacting Plasmon Nanoparticle Pairs: From Dipole−Dipole Interaction to Conductively Coupled Regime. *Nano Lett.* **2004**, 4, 1627-1631.

(22) Fan, J. A.; Wu, C.; Bao, K.; Bao, J.; Bardhan, R.; Halas, N. J.; Manoharan, V. N.; Nordlander, P.; Shvets, G.; Capasso, F., Self-Assembled Plasmonic Nanoparticle Clusters. *Science* **2010**, 328, 1135-1138.

(23) Tao, A.; Sinsermsuksakul, P.; Yang, P., Tunable plasmonic lattices of silver nanocrystals. *Nat. Nano.* **2007**, 2, 435-440.

(24) Dahmen, C.; Schmidt, B.; von Plessen, G., Radiation Damping in Metal Nanoparticle Pairs. *Nano Lett.* **2007**, 7, 318-322.

(25) Søndergaard, T.; Bozhevolnyi, S., Slow-plasmon resonant nanostructures: Scattering and field enhancements. *Phys. Rev. B* **2007**, 75, 073402.

(26) Nielsen, M. G.; Gramotnev, D. K.; Pors, A.; Albrektsen, O.; Bozhevolnyi, S. I., Continuous layer gap plasmon resonators. *Opt Express* 2011, 19, 19310-19322.

4. Fluorophores as Gain Media and their Incorporation into the Nanocube Metasurfaces

4.1 Introduction

The nanocube metasurfaces are able to confine light within the nanometer scale gap between the nanocubes and the metal substrate. This gap which is much smaller than the wavelength of the incident light at the metasurface's resonant frequency provides an opportunity for the production of nanoscale optical devices, such as lasers, light emitting diodes, optical sensors, and photodetectors. Devices such as lasers and LEDs have been shown to be realized by the incorporation of a gain medium into the cavity where the light in confined. A gain medium consists of a spontaneous photon emitter and in most cases is a fluorophore of some kind.[1] The location of the plasmonic modes can also provide enhancing effects on the properties of the gain medium. When the frequency of the plasmon resonance and the emission of the fluorophore are overlapped, an enhancement of the fluorescence intensity and a reduction of the fluorescence decay time is observed.[2] Intensity enhancement has potential applications in single molecule sensing,[3] and generally increases the signal to noise ratio of fluorescence based sensors. A decrease in the decay time of has the effect of having the fluorophore in the ground state faster and thus more often. This will reduce the effect of bleaching and allow for higher sensitivity when using fluorescence for concentration or time sensitive studies.

There are two major classes of fluorophores. The first being organic dye molecules and the second being quantum dots. Organic dyes have been thoroughly studied and have

the advantage of being easily purchased at virtually any wavelength within the visible range. Quantum dots while purchasable are cheaply made in a lab setting. They provide tunable fluorescence by changing quantum dot size, which can be changed by varying reaction parameters.[4] Quantum dots also have the advantage of having much longer photobleaching times, a factor that plagues organic dyes or proteins.[5] They also have faster decay times, usually in the picosecond range compared to nanoseconds for organic dyes.[6] Another advantage of quantum dots is their broad absorption range see figure 4.1, allowing for excitation from virtually any wavelength below the emission of the quantum dot.

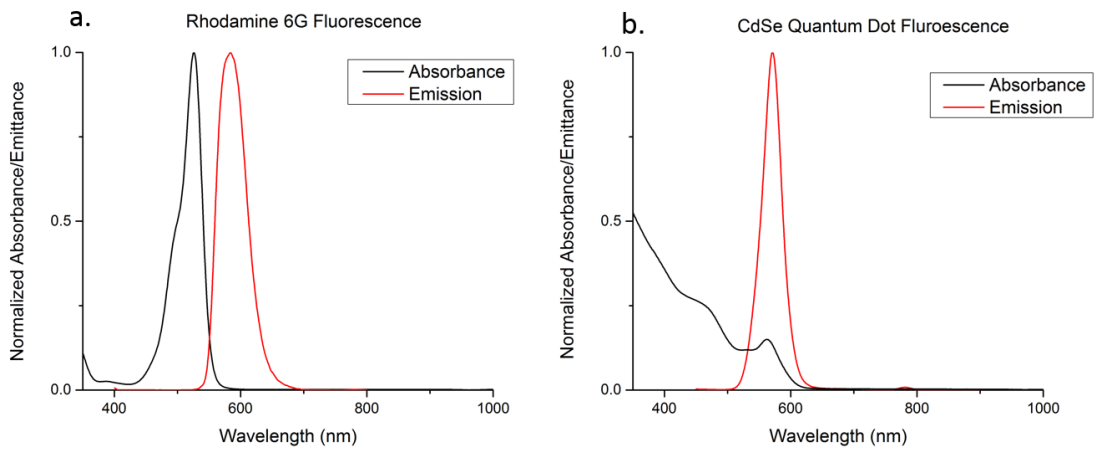

Figure 4.1. a) Absorption and photoluminescence spectra of rhodamine 6G. b) Absorbtion and photoluminescence of CdSe Quantum dots show their broad absorbance at wavelengths below the initial absorption peak.

In this work we have begun preliminary experiments involving the incorporation of the organic dye, rhodamine 6G, and CdSe quantum dots into the spacer layer of the nanocube metasurfaces. Experimental progress has been limited by complications with quantum dot synthesis as well as issues with both dye and quantum dot aggregation which will be illuminated in the following pages.

4.2 Methodology

Several methods of fluorescent particle placement have been attempted in this work. Initial work was done with rhodamine 6G (R6G). Spin coating was used to make a thinfilm of the dye on a silicon substrate. A 10^{-4} M Rhodamine 6G (Aldrich) with 1 wt% Poly(methyl methacrylate) (PMMA) (11.5K, Polymer Source) or 1 wt % Polystyrene (PS) (10.5K, Polymer Source) was first dissolved in chloroform or toluene and then made to fully wet a piranha treated silicon substrate. The substrate was then spun in a single step at 3000 rpm for 55 seconds. When PMMA was used the substrate was annealed at 110°C for one hour. Optical characterization was done with a standard optical microscope under 100x magnification. Colloidal photoluminescence measurements were performed on a Perkin-Elmer fluorimeter using a 390nm excitation. Substrate photoluminescence measurements were performed on a Renishaw inVia Raman system using a 488 nm laser and an appropriate filter for photoluminescence.

Cadmium Selenide Quantum dots were synthesis using previously reported methods.[7] Size tuning was done by changing the reaction time and reaction temperature. Emission peaks of ~580 nm were consistently synthesized at 280°C with reaction times of 5 minutes. Quantum dots of higher wavelength (redder) were attempted with little success. The quantum dots were washed several times by spinning in a centrifuge at 3000 rpm for 15 minutes in chloroform. At this point a visible organic layer would be removed, as well as any precipitate that forms. The remaining supernatant would then be mixed with an excess of acetone. Once in acetone spinning at 5000 rpm for 15 minutes was done in order to precipitate out all of the quantum dots. The supernatant was discarded and the precipitate

was dispersed in chloroform to begin the washing process again. Similar to the Rhodamine 6G the quantum dots were arrayed on the substrate using a spin coater. In this case no addition of polymer was used, colloidal QDs were spun. Silicon substrates were first piranha washed and then treated with hexamethyldisilazane (HMDS) to incur hydrophobicity. The quantum dots were spun at 3000 rpm for 55 seconds. Characterization was done in a similar manner to the R6G films. In addition scanning electron microscopy was used to further characterize the films.

4.3 Results and Discussion

We firsts examined the uniformity of polymer-dye films to check the efficacy for use as the spacer layer in the nanocube metafilms. Figure 4.2 shows optical microscopy images of the result of spin-coating PMMA and polystyrene (PS) with rhodamine 6G mixed in. From the figure 4.2 it can be seen that the R6G is crystallizing during the spin coating process. This prevents the formation of a uniform film as the crystals create areas of high fluorescence, while the rest of the polymer film has minimal fluorescence. This crystallization occurred in both PS and PMMA. It is believed that the crystallization is caused by poor solubility of the dye within the polymers. It is suspected that R6G is more soluble in PMMA due to its charged nature, though in literature it has been used both.[8,9]

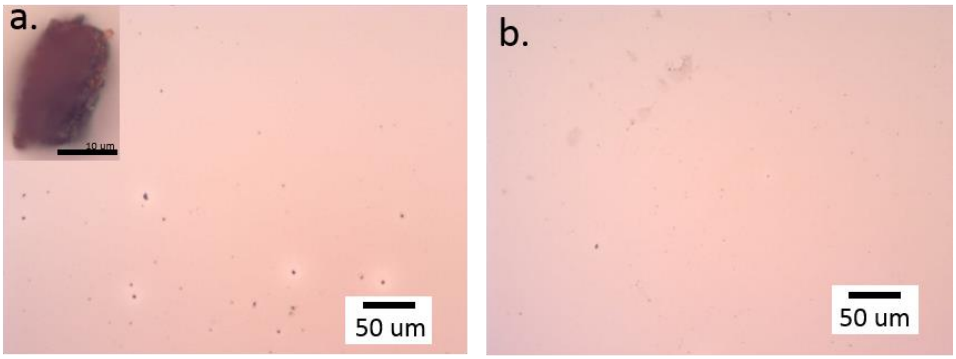

Figure 4.2. a) Optical microscope image of rhodamine 6G in PMMA that has been spun coated and annealed onto a silicon substrate under 10x magnification. Inset of a) shows a zoomed in (100x) image of one of the R6G crystals. B) Optical microscope image of rhodamine 6G in PS. It can be observed that crystallization is also present.

In order to reduce the crystallization of the dye better solubility of the dye would have to be accomplished. While not attempted others have add success by adding a small amount of methanol to the solution.[8] More sonication to ensure the solution is well mixed before the spin coating could also result in more uniformity.

Second because of their easily tunable nature quantum dots were explored instead of the rhodamine 6G. Initial synthesis results seems promising, though the washing procedure still needs to be optimized. Figure 4.3a shows a TEM image of the synthesized Quantum dots. It can be seen that large amount of excess of the organic capping ligand are still present in the sample. Regardless these quantum dots were spun onto silicon to gauge their ability to form uniform films. Figure 4.3bc shows an SEM and optical microscope images that indicate that like the R6G the quantum dots also aggregate when spin coating. In this case no enveloping polymer was used. Figure 4.3d indicates that very little fluorescence is not within aggregates on the film. Again limited solubility of the quantum

dots may be the primary cause of the aggregation. It is also possible that the capping ligand on the quantum dots is not stably bound resulting in aggregation. A solution to this issue may be a ligand exchange to an alkanethiol that will have a higher binding affinity and should result in less aggregation.

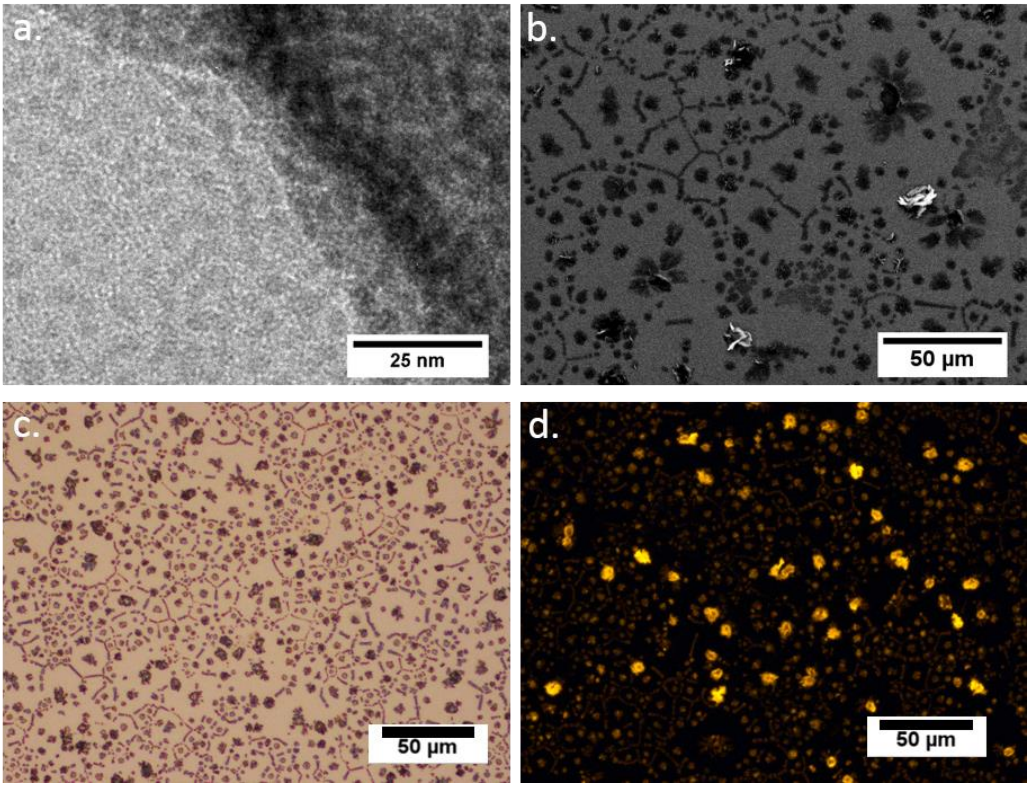

Figure 4.3. a) TEM image of CdSe QDs show there size of ~3.5 nm. Also visible is excess organics. b) SEM image of a spun coat QD film showing aggregation of the QDs and additional organic charging effects. c) Optical microscope image showing the QD aggregates. d) Fluorescence microscope image indicating that the QDs are located in the visible crystals.

4.4 Future Directions

Once a relatively uniform film of fluorophore has been fabricated, they will be incorporated into the nanocube metasurface. Additional tuning of the fluorescence and the

metasurface resonance will key as they need to overlap in order to see an enhancing interaction. Currently we have only explored CdSe quantum dots. These may not be able to achieve an emission that is of high enough wavelength. The synthesis of PbS quantum dots or the addition of a shell around the CdSe quantum dot have be shown to red shift the fluorescence.[10] Once the appropriate films have been fabricated the next challenge is characterization. In order to truly measure the enhancement of the fluorescence decay length a spectrometer capable of femtosecond excitation pulses will be required.

Once the effect of the film on the fluorophore is properly characterized, the lasing capability of the film will be explored. This may require defects purposely built into the film to allow the coherent light to escape the cavity. Different pumping schemes will need to be explored. Whether a laser is required, or if electrical pumping can be achieved.

4.5 Chapter 4 References

(1) Träger, F. Springer Handbook of Lasers and Optics, 2012, (xxxi, 1694 p.).

(2) Lu, D.; Kan, J. J.; Fullerton, E. E.; Liu, Z. Enhancing Spontaneous Emission Rates of Molecules Using Nanopatterned Multilayer Hyperbolic Metamaterials. *Nat. Nanotechnol.* **2014**, *9*, 48–53.

(3) Ambrose, W. P.; Goodwin, P. M.; Keller, R. a; Martin, J. C. Alterations of Single Molecule Fluorescence Lifetimes in near-Field Optical Microscopy. *Science* **1994**, *265*, 364–367.

(4) Leutwyler, W.; Bürgi, S.; Burgl, H. Semiconductor Clusters, Nanocrystals, and Quantum Dots. *Science* **1996**, *271*, 933–937.

(5) Chan, W. C. Quantum Dot Bioconjugates for Ultrasensitive Nonisotopic Detection. *Science (80-.).* **1998**, *281*, 2016–2018.

(6) Borri, P.; Langbein, W.; Hvam, J. M.; Heinrichsdorff, F.; Mao, M.-H.; Bimberg, D. Ultrafast Gain Dynamics in InAs-InGaAs Quantum-Dot Amplifiers. *IEEE Photonics Technol. Lett.* **2000**, *12*, 594–596.

(7) Khon, E.; Lambright, S.; Khon, D.; Smith, B.; O'Connor, T.; Moroz, P.; Imboden, M.; Diederich, G.; Perez-Bolivar, C.; Anzenbacher, P.; *et al.* Inorganic Solids of CdSe Nanocrystals Exhibiting High Emission Quantum Yield. *Adv. Funct. Mater.* **2012**, *22*, 3714–3722.

(8) Tou, T. Y.; Yap, S. S.; Chin, O. H.; Ng, S. W. Optimization of a Rhodamine 6G-Doped PMMA Thin-Slab Laser. *Opt. Mater. (Amst).* **2007**, *29*, 963–969.

(9) Mongy, E.; Abd, S. Preparation and Spectroscopic Studies of Rhodamine 6G Doped Polystyrene. *Aust. J. Basic Appl.* **2009**, *3*, 1954–1963.

(10) Bakueva, L.; Gorelikov, I.; Musikhin, S.; Zhao, X. S.; Sargent, E. H.; Kumacheva, E. PbS Quantum Dots with Stable Efficient Luminescence in the Near-IR Spectral Range. *Adv. Mater.* **2004**, *16*, 926–929.